"NEUTRINO COUNTING" IN e^+e^- ANNIHILATION*

DAVID L. BURKE

Stanford Linear Accelerator Center
Stanford University, Stanford, California, 94305

It is of great interest to study the process,

$$e^+e^- \rightarrow \text{weakly interacting particles} \tag{1}$$

shown schematically in Fig. 1(a). A final state that consists entirely of neutral particles that interact only weakly in matter is not directly observable in detectors normally used at e^+e^- colliding beam facilities, but we can infer the existence of such processes by detecting events accompanied by initial-state radiation of a single, hard photon [Fig. 1(b)],

$$e^+e^- \rightarrow \gamma + \text{weakly interacting particles.} \tag{2}$$

The study of single-photon production in e^+e^- annihilation was first proposed by Ma and Okada[1] as a means of determining the number of massless neutrino species, but as we will discuss, measurements of single-photon rates and spectra will have implications for many theoretical ideas.
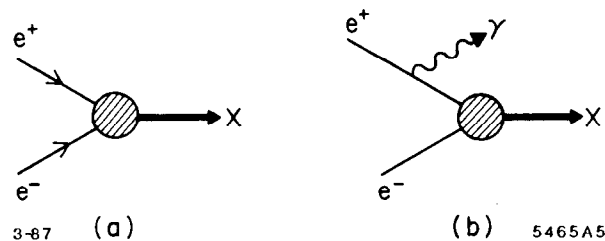

Fig. 1. (a) Schematic diagram of production of weakly interacting particles by e^+e^- annihilation. (b) Radiative correction to e^+e^- annihilation.

The first of these two lectures will start to examine what we can learn from studies of reaction (2). We will see that the physics probed by this reaction depends greatly upon the energy at which experiments are done. Most of this lecture, however, will focus on the experimental techniques used for these studies, and in particular, on the central problem of electromagnetic calorimetry. The second lecture will discuss the present status of our knowledge of single-photon production with a detailed look at the ASP experiment at PEP, and the physics interpretation of the results of that experiment. We will then go on to look at how experiments will be done at the next generation of e^+e^- machines SLC and LEP, and examine the importance of making a precise measurement of the cross section for reaction (2) at center of mass energies near the mass of the Z^0.

1. NEUTRINO COUNTING AND EXPERIMENTAL TECHNIQUES

1.1 Physics Below the Z^0 Mass

The standard electro-weak processes shown in Fig. 2 contribute to reaction (2) with the differential cross section,[2]

$$\frac{d^2\sigma}{dp_t^\gamma d\cos\theta_\gamma} = \frac{G_F^2\alpha}{6\pi^2} \cdot \frac{s(1-x_\gamma)}{p_t^\gamma \sin^2\theta_\gamma} \cdot \left[(1 - \frac{1}{2}x_\gamma)^2 + \frac{1}{4}x_\gamma^2\cos^2\theta_\gamma\right]$$

$$\cdot \left\{\frac{M_Z^4\{N_\nu(g_V^2 + g_A^2) + 2(g_V + g_A)[1 - s(1-x_\gamma)/M_Z^2]\}}{[s(1-x_\gamma) - M_Z^2]^2 + M_Z^2\Gamma_Z^2} + 2\right\}, \quad (3)$$

where p_t^γ is the momentum transverse to the beam line of the detected photon, θ_γ is the polar angle of the detected photon, $x_\gamma = 2E_\gamma/\sqrt{s}$, $g_V = -\frac{1}{2} + 2\sin^2\theta_W \approx -.05$, $g_A = -\frac{1}{2}$, and N_ν is the total number of massless neutrino species that are produced through the Z^0 propagator. At center of mass energies far below the Z^0 mass the visible part of the cross section is unfortunately quite small. Notice that the photon distribution $E_\gamma^{-1}\sin^{-2}\theta_\gamma$ (a characteristic bremsstrahlung spectrum) is peaked at low energies and at polar angles near to the beam line. For example at PEP ($\sqrt{s} = 29$ GeV) the detectable cross section with $E_\gamma > 1$ GeV and $\theta_\gamma > 20°$ is about 0.04 pb (if $N_\nu = 3$). So with an integrated luminosity of 100 pb^{-1} (typical of PEP and PETRA experiments), and 50% analysis efficiency, we expect to see only 2 or 3 events. These experiments will not actually determine the value of N_ν, but they will place interesting limits on this quantity.

While it is unfortunate that the known Standard Model contributions to reaction (2) are small at $\sqrt{s} \ll m_Z$, the lack of a known physics background to this final state makes it an ideal place to look for new phenomena. The most prominent example of possible contributions to the signal are reactions predicted
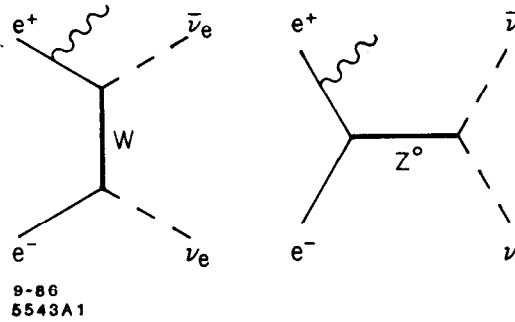
2

9-86
5543A1

Fig. 2. Production of neutrino pairs by charged and neutral weak currents in e^+e^- annihilation.

to occur by theories of supersymmetry (SUSY) such as those shown in Fig. 3. The rates for all of these processes depend in detail on the SUSY mass spectrum and various mixing parameters.[3] The particular case of a model in which the photino $\tilde{\gamma}$ is a mass eigenstate and is the lightest SUSY particle is interesting because it leads to the purely electromagnetic process shown in Fig. 3(a). The cross section for this process in the limit $m_{\tilde{\gamma}} \ll \sqrt{s}$ is,

$$\frac{d^2\sigma}{dp_t^\gamma d\cos\theta_\gamma} = \frac{2\alpha^3}{3} \cdot s \cdot \left(\frac{1}{m_{\tilde{e}_R}^4} + \frac{1}{m_{\tilde{e}_L}^4}\right) \cdot \frac{1}{p_t^\gamma \sin^2\theta_\gamma} \cdot f(E_\gamma, \cos\theta_\gamma) \qquad (4)$$

This cross section is large for light photinos and selectrons, and becomes comparable to the weak cross section (3) only for $m_{\tilde{e}_R}$ and $m_{\tilde{e}_L}$ comparable to the W mass. The range of parameter space that an experiment at PEP or PETRA can explore[4] is shown in Fig. 4.
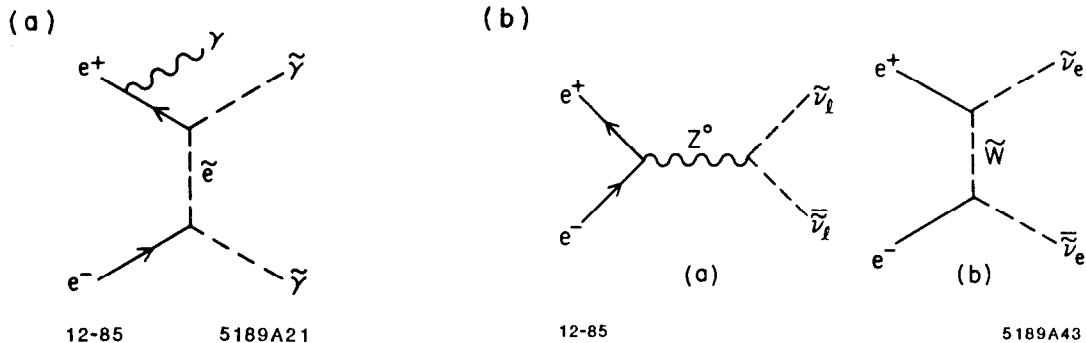
(a)

(b)

12-85   **5189A21**   **12-85**   **5189A43**

Fig. 3. Processes predicted to exist in theories of Supersymmetry. (a) $e^+e^- \longrightarrow \gamma\tilde{\gamma}\tilde{\gamma}$, (b) $e^+e^- \longrightarrow \gamma\tilde{\nu}\tilde{\bar{\nu}}$.
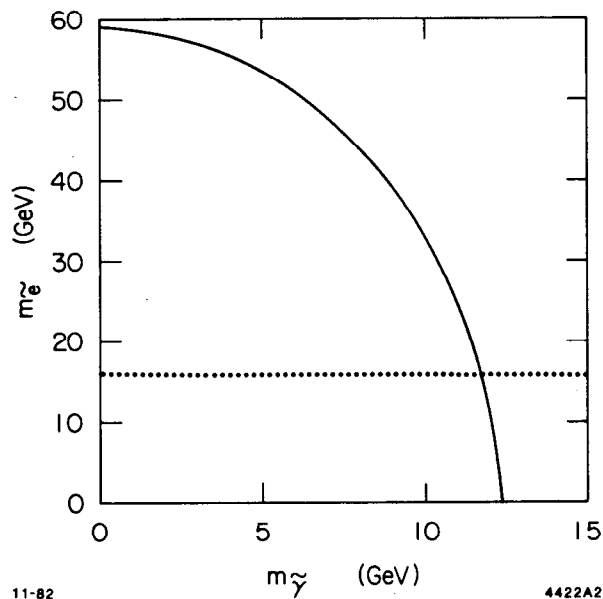
Fig. 4. Range of $m_{\tilde{e}}$ and $m_{\tilde{\gamma}}$ that could be explored in a search
for single-photon events in e^+e^- annihilation at $\sqrt{s} = 29$ GeV
with an integrated luminosity of 100 pb^{-1}.

It is interesting to think about the behaviour of the photino as it passes
through matter. Will it leave any signal in a detector? Probably not. The
possible interactions that the $\tilde{\gamma}$ would have with electrons and quarks, shown
in Fig. 5, will always involve a propagator of another supersymmetric particle.
These reactions will be suppressed to weak scales[5] unless the mass of either the
selectron or at least one squark is small (e.g., $m_{\tilde{q}} \ll m_W$). Unambiguous limits
on the masses of scaler quarks are surprisingly difficult to find, but the absence of
an entire spectrum of supersymmetric hadrons requires these masses to be larger
than a few GeV. This is not sufficient to make the photino truely a "neutrino-like"
particle, but the lack of any evidence for light squarks leads us to assume that
the photino would not undergo interactions with large probability as it passes
through components of detectors.

The energy dependences of the cross sections (3) and (4) for neutrino pro-
duction and the $\gamma\tilde{\gamma}\tilde{\gamma}$ SUSY process are shown[6] in Fig. 6. Notice that PEP is
perhaps the best place to search for electromagnetic SUSY interactions, while
experiments at SLC and LEP will be blessed with a large neutrino cross section
near the Z^0 pole. At the intermediate energy of 60 GeV where TRISTAN will op-
erate there could be some confusion. The neutrino cross section (3) of ≈ 0.15 pb
($N_\nu = 3$) will result in 10 to 20 events per 100 pb^{-1}, so it will require large
integrated luminosities to be sensitive to additional contributions. It will still
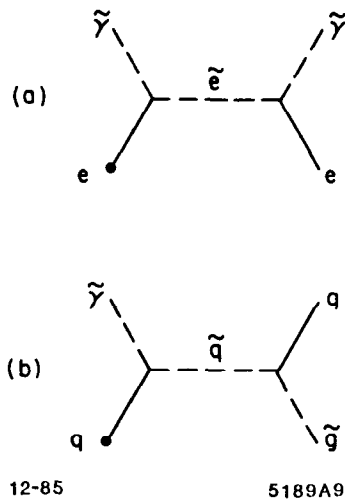
(a)

(b)

12-85   5189A9

Fig. 5. Interactions of a photino with (a) an atomic electron, and (b) nuclear quarks.
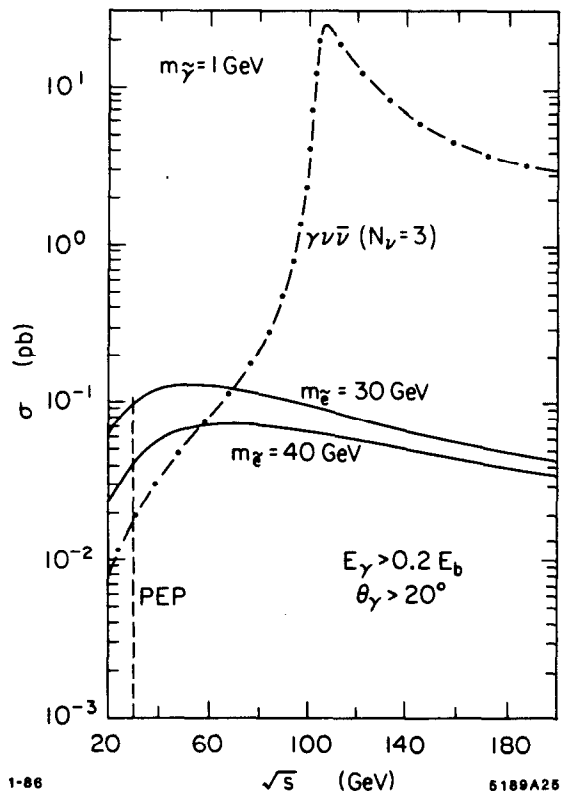

1-86 $\sqrt{s}$ (GeV)   5189A25

Fig. 6. Comparison of cross sections for $\gamma \nu \bar{\nu}$ and $\gamma \tilde{\gamma} \tilde{\gamma}$. The peak of the $\gamma \nu \bar{\nu}$ cross section is shifted by the requirement $E_\gamma > 0.2 E_b$.

5

be important to do this measurement at TRISTAN, however, since we will want as complete a picture of the energy dependence of the cross section as possible. Notice, for example, that while the range of $m_{\tilde{z}}$ is not greatly extended beyond that explored at PEP and PETRA, the higher beam energy will make it possible to produce photinos of nearly twice the mass that can be generated at the lower energy machines.

1.2 Neutrino Counting Near the Z^0

Each species of massless Dirac neutrino will generate a partial width for the Z^0 that is given approximately by,[2,7]

$$\Gamma_{Z^0 \to \nu\bar{\nu}} = \frac{G_F m_Z^3}{12\pi\sqrt{2}} \; .$$ (5)

If we take $m_Z = 93$ GeV/c^2, then (5) corresponds to a partial width of 0.175 GeV or about 6% of the total Z^0 width. If the number of neutrino generations is three, then $\approx$ 18% of all produced Z^0's will decay to neutrino pairs. Since experiments at SLC and LEP expect to obtain data samples that consist of $\geq 10^6$ produced Z^0's, we can anticipate that measurements in the near future will yield a fundamental feature of nature — the number of weak isospin generations.

We will discuss this topic in much greater detail in the second lecture, but I'll emphasize at this point that the partial width of the Z^0 to weakly interacting particles need not be quantized! For example, here is a list of the contributions that various kinds of possible final states would make to the Z^0 width ($\beta = (1 - 4m^2/s)^{\frac{1}{2}}$ is the velocity of pair-produced particles):

- Massive Dirac neutrinos $1.5\% \cdot \beta(3 + \beta^2)$
- Massive Majorana neutrinos $6\% \cdot \beta^3$
- Scalar neutrinos $3\% \cdot \beta^3$
- Neutralinos 0% to $\approx 10\%$

Notice that the Z^0 partial decay widths for these particles can take on essentially any values, and that no unambiguous limits exist on any of their masses. The suppression by kinematics of the production rates of several of these particles is not necessarily small. The β^3 factor, shown in Fig. 7, heavily suppresses production of particles with mass $\geq$ 25-30 GeV/c^2. It is even possible that the detected photon will not be radiated by one of the initial-state leptons. The production of Higgsinos $\tilde{\chi}_i^0$ and $\tilde{\chi}_j^0$ followed by the decay of the more massive of the two would proceed as shown in Fig. 8 if these are the lightest supersymmetric particles. The effect of this process on the total Z^0 width might be small, but

because the produced photon spectrum is generally quite broad in the labora-
tory (in detail it depends on the masses of $\tilde{\chi}_i^0$ and $\tilde{\chi}_j^0$), its contribution to the
observed single-photon final state could be significant. Interestingly, the mass
of the neutralino state $\tilde{\chi}_j^0$ that can be produced in this decay is not limited by
$m_{Z^0}/2$. Precise and careful measurements of the cross section for reaction (2) at
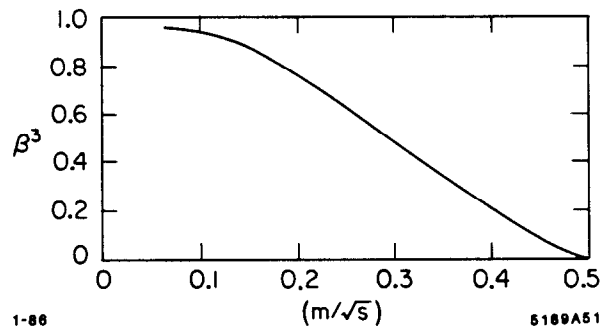the SLC and LEP will be sensitive to a number of possible new phenomena.

Fig. 7. The β^3 threshold factor for production of scalar
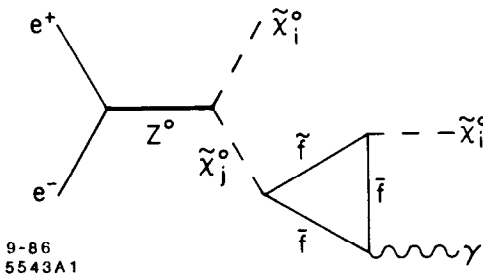particles by e^+e^- annihilation.

Fig. 8. Single-photon production in the decay of a
neutralino. The particle $\tilde{\chi}_i^0$ is assumed to be the lightest
supersymmetric particle, and is therefore stable.

1.3 Experimental Considerations

The single-photon final state does not offer much of an experimental signa-
ture. There are only two features — a photon and nothing else. This may seem
to be a trivialization of the experiment, but it emphasizes the need to recon-
struct both parts of the signature. First we must find a photon, then we must
be sensitive to any other particle that might be produced in association with it.

Backgrounds to the signal that we are looking for can be generated by other e^+e^- processes, cosmic rays, beam-gas collisions, and debris from interactions of stray beam particles with machine components.

Backgrounds produced by the beam-beam collision can be eliminated by noticing that once we have detected a photon we can be assured that there must be something else produced in the interaction that balances the momentum transverse to the beam line. For example, the most copious and difficult background to the signal comes from radiative Bhabha scattering,

$$e^+e^- \rightarrow e^+e^-\gamma \tag{6}$$

when both of the final state leptons escape detection. But if we require that the transverse momentum of the photon, p_t^γ, be larger than some minimum value, $p_{t\min}^\gamma$, then at least one of the leptons must appear at a polar angle larger than

$$\theta_{\text{veto}} = \frac{p_{t\min}^\gamma}{2 \cdot E_b} \quad , \tag{7}$$

where E_b is the energy of the beam (Fig. 9). For example, if we wish to count single-photon events with p_t^γ greater than 1 GeV/c at PEP then we must build a detector that will find all charged particles and photons with θ above 35 mr. This can be done, and we will discuss such a detector in Lecture II.
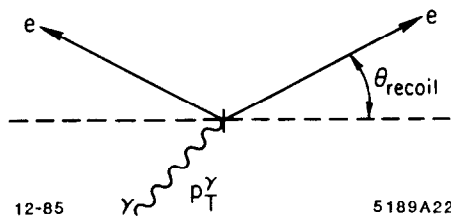

Fig. 9. Radiative Bhabha scattering.

There is an ultimate limit to how small p_t^γ can be before a background appears. Collisions of electrons with residual gas molecules inside the beam-pipe will result in the photoproduction of all-neutral final states (Fig. 10). Photons from decays of π^0's can counterfeit the signature that we are looking for. In this case the transverse momentum of the photon is taken up by a slow neutron which escapes detection. Fortunately this background is very forward-peaked, and the transverse momentum distribution of photons in the final state falls rapidly with little population above $p_t^\gamma \approx 0.5$ GeV/c. We will see this background when we
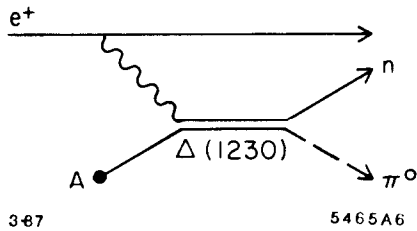
Fig. 10. Photoproduction of the $\Delta(1230)$ resonance by
the equivalent photon flux of the electron beam striking
a nucleus in the residual gas inside the beam pipe.

discuss the ASP experiment. Before we get to that discussion, however, we need
to understand how to detect a photon in the first place.

1.4 Electromagnetic Calorimetery[8]

When a photon with energy $E \gg m_e$ enters a region filled with a non-vacuous
medium it generates a shower of lower energy electrons, positrons, and photons
as depicted in Fig. 11. As the multiplicity of particles in the shower grows, the
mean energy of each particle decreases. The total energy in the shower also de-
creases as energy is lost by the charged-particle component through ionization of
the atoms in the medium. Eventually all of the incident particle's energy is lost to
the medium and the shower dissipates. Photons produced in high energy physics
experiments are almost always detected by observing the electromagnetic shower
that they create in one kind of total-absorption calorimeter or another. To under-
stand how these devices work we first look at the physics of an electromagnetic
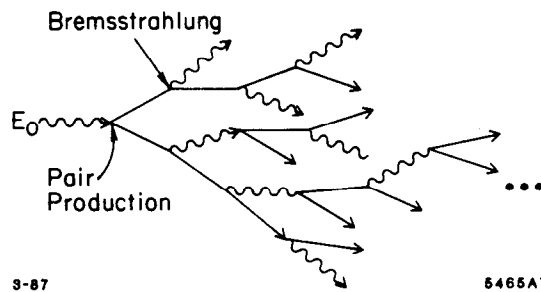shower in more detail.

Fig. 11. Schematic picture of an electromagnetic shower
initiated by a photon of energy E_0.

9

a. Bremsstrahlung

The lowest order electromagnetic interaction of an electron or positron with a nucleus of charge Z is the bremsstrahlung process shown in Fig. 12. This occurs with cross section,

$$d\sigma = 4\alpha Z^2 r_e^2 \cdot \left(\frac{dk}{k}\right) \cdot f(E,k,Z) \qquad (8)$$

where E and k are the laboratory energies of the incident lepton and outgoing photon respectively, and the nucleus is treated as a point-particle of charge Z. The factor $f(E,k,Z)$ results from the integration over the photon propagator q from q_{min} to q_{max}. In particular,

$$f \sim \ln(q_{max}/q_{min}) \cdot \qquad (9)$$

The upper limit q_{max} is set by kinematics and is relatively unimportant, while q_{min} is determined by the screening of the nuclear charge at large impact parameters, and defines the behaviour of the cross section as a function of the incident particle's energy.
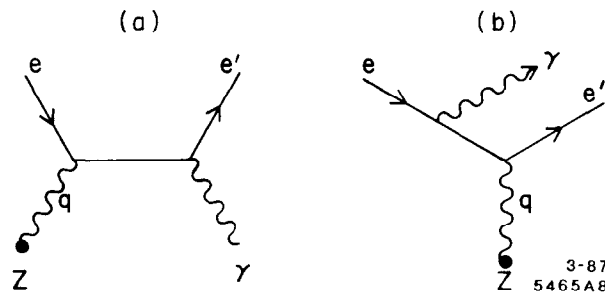

Fig. 12. Lowest order diagram for the radiation of a photon in the scattering of an electron from a nuclear charge (bremsstrahlung).

The atomic screening effect is depicted in Fig. 13. At non-relativistic velocities the electromagnetic fields of the incident particle are hardly different from those of a static charge, but at velocities near to the speed of light the retarded potentials conspire to produce fields that extend over a much larger range of impact parameter. So q_{min} becomes smaller and the total cross section grows as the incident particle energy is increased. This doesn't persist indefinitely, however, because eventually the maximum effective impact parameter exceeds the Bohr radius of the atom and the atomic electrons begin to screen the nuclear charge

10

from the incident particle. At this point $q_{\min}$ becomes a constant given by the atomic size. In the extreme relativistic limit (the so-called complete-screening limit),

$$f(E,k,Z) \longrightarrow \left[1 - \frac{2}{3}\frac{E'}{E} + \left(\frac{E'}{E}\right)^2\right] \cdot \ln(183 \cdot Z^{-1/3}) \tag{10}$$

Notice that $Z^{-1/3}$ is just the scaling factor of the atomic radius. The value 183 is, in the final accounting, a convention that leads to a good fit to data. It is convenient to define the radiation probability per unit path length for the incident lepton,

$$\phi_{\text{rad}}\, dx\, dk = 4\alpha \left(\frac{N_a}{A}\right) Z^2 r_e^2 \left[1 - \frac{2}{3}\cdot\frac{E'}{E} + \left(\frac{E'}{E}\right)^2\right] \cdot dx \left(\frac{dk}{k}\right)$$
$$\cdot \ln\left(183 Z^{-1/3}\right) \tag{11}$$

where N_a is Avagadro's number (N_a/A is the number of atoms per gram of material), and dx is the path length element measured in units of gm/cm^2. This is a natural unit in which to define the interaction probability since it removes some of the dependence on the density of the medium, but notice that it represents a different spatial distance in different materials.
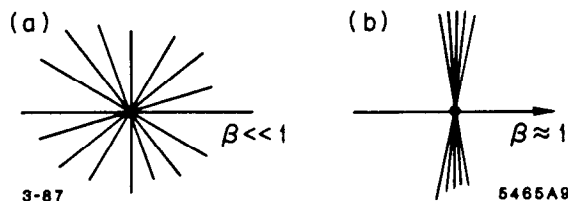

Fig. 13. Electric field lines surrounding a charge, (a) moving slowly in the laboratory, and (b) with relativistic velocity in the laboratory.

b. Radiation Length

The value of ϕ_{rad} is numerically very large, so an electron (or positron) will radiate many low-energy photons as it passes through matter. It is reasonable, then, to compute from (11) the average energy lost by an electron per unit gm/cm^2,

$$\bar{E}_{\text{rad}}(E) = \int\limits_{0}^{E} k \, \phi_{\text{rad}}(E, k) dk$$

$$= 4\alpha \left(\frac{N_a}{A}\right) Z^2 r_e^2 E \cdot \ln(183 \, Z^{-1/3}) \equiv E/X_0 \qquad (12)$$

where we have defined the *radiation length* of the material in the last line,

$$\frac{1}{X_0} = 4\alpha \left(\frac{N_a}{A}\right) Z^2 r_e^2 \cdot \ln(183 \, Z^{-1/3}) \qquad (13)$$

In terms of X_0 the mean energy of an electron with initial energy E_0 is given at depth x by,

$$\bar{E}(x) = E_0 \, e^{-x/X_0} \quad . \qquad (14)$$

This remarkably simple form is due to the lack of any energy dependence in expression (13) for the radiation length in the complete-screening limit. It turns out that this approximation is quite good even for relatively low-energy electrons. As we will see, most of the dependence of the development of an electromagnetic shower on the medium in which it is propagating can be removed if distances are measured in units of radiation lengths, and Eq. (14) will largely determine the longitudinal distance over which a shower will extend.

Asymptotic screening of the radiation cross section is one feature of the interaction of an electron with bulk matter that is important to the behaviour of electromagnetic showers; the $1/k$ photon spectrum of the bremsstrahlung process is another. This spectrum is characterized by the fact that equal numbers of photons will be emitted in geometric intervals of energy, *i.e.*, N_γ(100-200 MeV) = N_γ(200-400 MeV) = etc. In a practical sense this results in two cases of interest; (1) emission of low-energy photons in large numbers, and (2) emission of a few high-energy photons. The first case can be approximated as a continuous energy loss by the electron and is the process that we discussed above, while the second category can be considered as consisting of a set of discrete events. These are the processes that produce more shower particles and thus propagate the shower as we depicted in Fig. 11. We need to parameterize a boundary between these two classes. Such a boundary is created naturally by the competing continuous loss of energy through ionization of the atoms in the medium.

c. Ionization Loss and Critical Energy

The interaction of a massive charged particle with atomic electrons (Fig. 14) occurs with probability per gm/cm^2 given by,

$$\phi_{\text{ion}}(E,k)\, dx\, dk = 2\pi \left(\frac{N_a}{A}\right) Z r_e^2 \cdot \left(\frac{m_e}{\beta^2}\right) \cdot \left(\frac{dk}{k^2}\right) \cdot dx \qquad (15)$$

The variables E and k in this expression are the laboratory energies of the incident particle and scattered electron respectively. (Incident electrons are not massive enough for this formula to be correct for them at all energies. We will come back to this point shortly.) The so-called "knock-on" probability to produce a free electron at a large value of k is heavily suppressed, but the total interaction probability is extremely large. As for the case of bremsstrahlung losses, we compute the average energy loss per gm/cm^2,

$$-\frac{\overline{dE}}{dx} = \int_{k_{\min}}^{k^{\max}} k\; \phi_{\text{ion}}(E,k) dk$$

$$= 2\pi \left(\frac{N_a}{A}\right) Z r_e^2 \cdot \left(\frac{m_e}{\beta^2}\right) \cdot \ln(k_{\max}/k_{\min}) \qquad (16)$$

In the jargon of the experimentalists this is often referred to as the "dE/dx" energy loss of a particle passing through a medium. The minimum energy that can be lost in a single collision, $k_{\min}$, is set by the minimum atomic ionization potential $I(Z)$. At high energies E, this minimum transfer occurs at impact parameters that are larger than the interatomic spacing of the medium. Polarization of intervening atoms will effectively screen the target atom just as the atomic electrons screen the nuclear charge. As a result, the energy loss due to ionization becomes nearly constant at high energy. The actual mean energy loss per gm/cm^2 is shown in Fig. 15 for aluminum and lead media. The β^{-2} dependence at non-relativistic velocities is evident, as is the fully-screened uniform region at large velocities ($\gamma\beta > 100$). There is a shallow minimum at $\gamma\beta$ near unity followed by a slight rise as the range of the interaction grows due to the flattening of the electromagnetic fields created by the incident particle (Fig. 13).

It is important to notice several things in Fig. 15. Firstly, the β^{-2} section of the curve at $\gamma\beta < 1$ is not applicable for incident electrons. Slowly moving electrons are scattered through large angles by the basic interaction (Fig. 14), and are brought to rest locally. Secondly, the ionization process generates free non-relativistic (essentially thermal) electrons in the medium, and it is these particles that will create signals in detectors. Finally, it is most important to
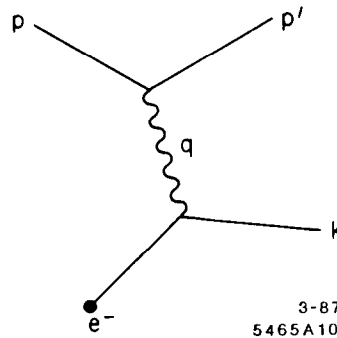
p ⟍   ⟋ p'

q

k

e⁻

3-87
5465A10

Fig. 14. Scattering of a massive charged
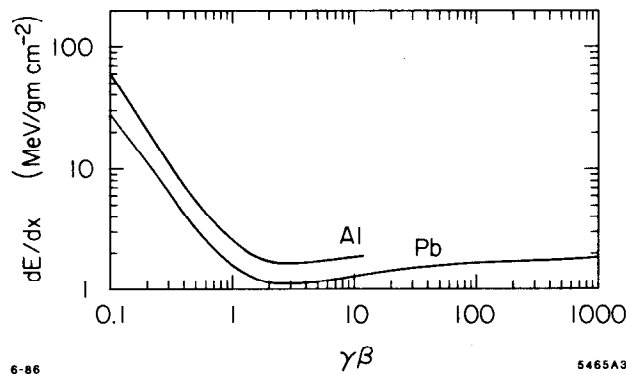particle by atomic electrons.

Fig. 15. Mean energy loss per gm/cm^2 of traversed ma-
terial suffered by a massive charged particle in
aluminum and lead media.

compare the rate of ionization loss suffered by electrons and positrons with the
loss of energy that they suffer through radiation. This is done in Fig. 16. Notice
that there is a particular energy, ϵ_c, called the critical energy, below which the
ionization loss quickly dominates the loss due to radiation. This value depends
upon the medium, but is typically 5-50 MeV in most common materials. The
significance of the critical energy is that shower particles with energy E greater
than ϵ_c can effectively propagate the shower, while particles with E less than
ϵ_c quickly lose their energy to ionization of the medium and are lost from the
shower. This is the boundary that we were looking for.

d. Pair Production

Photons propagating in an electromagnetic shower do not contribute directly
to the signal seen in detectors, and the only significant interaction they undergo
is the pair production process shown in Fig. 17. Electron-positron pairs are
produced when the photon interacts with the nuclear charge. The cross section
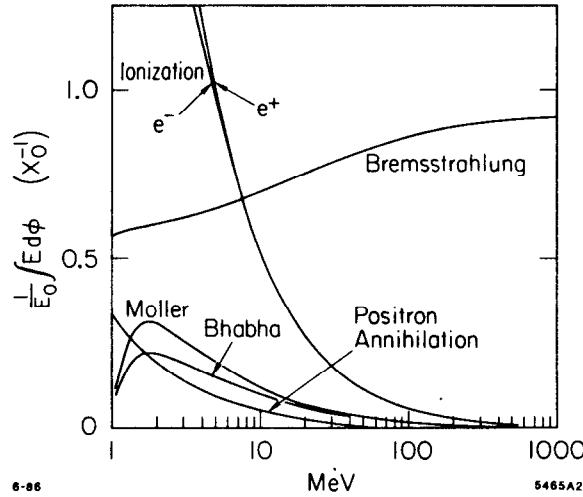
Fig. 16. Comparison of the mean energy lost by electrons and positrons by radiation with the loss due to ionization of the medium (lead).
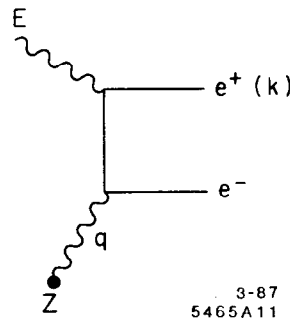

Fig. 17. Production of an electron-positron pair by the interaction of a photon with nuclear charge.

is screened by the charge of the atomic electrons just as the bremsstrahlung interaction. The cross section is,

$$\phi_{\text{pair}}(E,k)\,dx\,dk = 4\alpha \left(\frac{N_a}{A}\right) Z^2\, r_e^2 \cdot \left(\frac{dk}{E}\right) \cdot F(E,k) \qquad (17)$$

and in the high energy limit,

$$F(E,k) \longrightarrow \left[\left(\frac{k}{E}\right)^2 + \left(1 - \frac{k}{E}\right)^2 + \frac{2}{3} \cdot \left(\frac{k}{E}\right) \cdot \left(1 - \frac{k}{E}\right)\right] \cdot \ln(183\ Z^{-1/3}) \quad (18)$$

We compute the total conversion probability per unit length by integration over

15

the laboratory energy of one of the outgoing electrons,

$$\phi_{\text{pair}}\, dk = \frac{7}{9} \cdot \frac{1}{X_0} \ . \tag{19}$$

So we find that the photon mean free path is $\approx$ 9/7 of an electron radiation length. The exact value of ϕ_{pair} is shown in Fig. 18 (for lead). What we have found is that the interactions of electrons and photons that are responsible for the development of an electromagnetic shower are both characterized simply by the radiation length in a given medium. If we use the radiation length as our unit of distance, then we will be able to parameterize the properties of showers independently of the medium. We can even go a bit further by noticing that the photon mean free path and the electron radiation length are nearly equal, so we should expect that the number of hard photons in a well-developed shower will be approximately equal to the number of electrons in the shower.
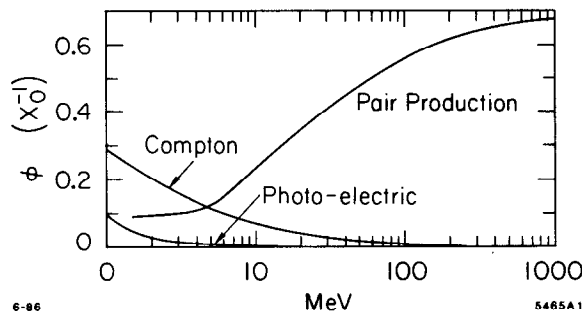

Fig. 18. Pair-production cross section in lead.

e. **Shower Development**

We can now construct a fairly simple, intuitive picture of the longitudinal development of an electromagnetic shower. We ignore all but the bremsstrahlung and atomic ionization processes for the charged-particle component, and consider only the pair-production interactions of photons. We express all cross sections in units of the radiation length in the medium, and use the asymptotic fully-screened values. We expect the number of particles in the shower to grow until the mean energy of the particles is equal to the critical energy of the medium and then to dissipate. This leads to the "universal shower curve" sketched in Fig. 19. We need only determine the depth t_{max} at which the shower peak occurs and the number of particles at the peak $N(t_{\text{max}})$. Let's make some guesses. Firstly, since we have said that the shower grows until the mean energy of the particles in the

shower reaches the critical energy it is not difficult to estimate that

$$N(t_{\max}) \propto \frac{E_0}{\epsilon_c} \ .$$

(20)

We might also expect the shower to reach its peak when the incident particle no longer is able to generate secondary particles with energies sufficient to further propagate the shower. This occurs when the incident particle energy is reduced to the critical energy,

$$\epsilon_c = E_0 \ e^{-t_{\max}}$$

or,

$$t_{\max} \sim \ln \frac{E_0}{\epsilon_c},$$

(21)

with t is measured in radiation lengths. We can already learn a great deal from this simple picture. The linear relation between the number of particles in a shower and the incident particle energy makes it possible to build detectors that can measure the energy of an electron or photon with good resolution and small systematic errors. The fact that the penetration depth of a shower grows only logarithmically with incident energy is also important since it means that calorimeters need not be physically very deep to provide measurements over a large range of energy.

6-86   5465A4
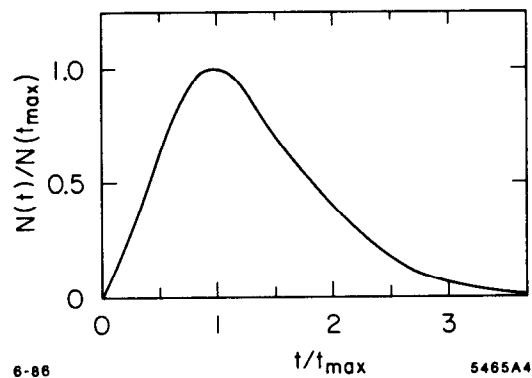
Fig. 19. Universal shower curve. The parameter t is the longitudinal depth in the shower measured in radiation lengths and $N(t)$ is the number of particles in the shower at depth t.

More sophisticated analytical models of shower development are formulated[9] as sets of evolution equations,

$$\frac{de}{dt} = \int\limits_{E}^{\infty} \left[e(E',t)\, P_{e\to e}\,(E',E) + \gamma\,(E',t)\, P_{\gamma\to e}(E',E) \right]\, dE'$$

$$- e(E,t) \int\limits_{0}^{E} P_{e\to e}\,(e,E')\, dE', \qquad\qquad (22a)$$

and,

$$\frac{d\gamma}{dt} = \int\limits_{E}^{\infty} \left[e(E',t)\, P_{e\to\gamma}\,(E',E) + \gamma(E',t)\, P_{\gamma\to\gamma}\,(E',E) \right]\, dE'$$

$$- \gamma(E,t) \int\limits_{0}^{E} \left[P_{\gamma\to e}\,(E,E') + P_{\gamma\to\gamma}\,(E,E') \right]\, dE' \ . \qquad (22b)$$

where $e(E,t)dE$ and $\gamma(E,t)dE$ are the number of charged particles and photons with energy E at depth t in the shower, and $P_{e\to e}(E',E)dE'$ is the probability that an electron of energy E' will produce an electron of energy E in length dt (bremsstrahlung and ionization processes), and $P_{\gamma\to e}(E',E)$, $P_{e\to\gamma}(E',E)$ and $P_{\gamma\to\gamma}(E',E)$ are similar functions that represent pair-production, bremsstrahlung, and Compton scattering processes.

In present-day language Eq. (22) along with the splitting-functions $P_{e\to e}$, $P_{e\to\gamma}$, $P_{\gamma\to e}$, $P_{\gamma\to\gamma}$ describe a fragmentation process. These equations can be solved analytically under the specific approximations:

(i) The Compton process can be ignored.

(ii) The remaining cross sections are completely screened.

(iii) The ionization energy loss rate is constant for charged-particles with $E > \epsilon_c$, and particles with energy less than the critical energy are assumed to simply deposit their energy locally in the medium.

The solution to the evolution equations then yields the universal shower curve of Fig. 19 with the parameters,[10]

	Primary $e^{\pm}$	Primary γ
$t_{\max}$	$\ln(E/\epsilon_c) - 1$	$\ln(E/\epsilon_c) - \frac{1}{2}$
$N_{\max}$	$0.1 \cdot (E/\epsilon_c)$	$0.1 \cdot (E/\epsilon_c)$
S	E/ϵ_c	E/ϵ_c

where S is the total charged-particle path length in the shower. Notice that

showers initiated by photons develop a little more slowly, and that S and N_{max} are proportional to E. These results are remarkably similar to the intuitive guesses that we made earlier.

The thoroughly modern approach to the electromagnetic shower problem is to use complete Monte Carlo simulations[11] that include exact forms of all sub-processes, and that allow geometric boundaries of different media to account for experimental detector elements. The path of each particle in the shower is traced from the point at which it is created until its energy drops below a particular cut-off which is typically set below the critical energy in each medium. Particles with energy below the cut-off E_{cut} are assumed to deposit their kinematic energy locally in the medium of the detector. The results of calculations of this sort for primary electrons (with $E_{cut} = 1$ MeV) can be summarized by,[10]

t_{max}	$1.1 \cdot \ln E - 0.25 \cdot \ln E_{cut} - 3.87$
N_{max}	$0.006 \cdot E + 3.1$
S	$0.65 \cdot (E/\epsilon_c)$
ΔS_{RMS}	$0.05 \cdot \sqrt{E}$

Notice that ΔS_{RMS} is the inherent fluctuation from shower to shower in the total charged-particle path length. This is a statistical process and the dependence on energy just reflects the expected $\sqrt{N}$ fluctuation in the number of particles in the shower. This gives the optimal *resolution* of a shower detector,

$$\frac{\Delta S_{RMS}}{S} \approx \frac{1\%}{\sqrt{E}} \tag{23}$$

that can be achieved if we are able to detect the complete charged-particle path length in each shower.

f. Electromagnetic Calorimeters

As a first attempt to design an electromagnetic calorimeter consider the apparatus shown in Fig. 20. A photon of energy 1 GeV that strikes the lead block will deposit all of its energy in the material and will raise the average temperature of the block by 1.2×10^{-13} degrees Celsius. The thermometer will register this increase, and if the physicist's eye is sufficiently sharp, then the photon's presence will be known and its energy measured. All of the elements of a real detector exist in this example: (1) an absorber, (2) a sensor, and (3) a read-out technique. This system has the advantage that the recorded temperature rise will be proportional to the energy of the incident particle, and since the system is sensitive to the complete charged-particle path length in the shower it inherently could achieve the optimal resolution [Eq. (23)] possible for a detector. There are,

however, several problems with this device. The system produces an extremely small signal. Errors in reading the temperature rise, small air currents in the room, and other factors will result in changes in the thermometer reading that are large compared to the expected signal. It is important to optimize the *signal-to-noise* ratio in real detectors. The read-out is slow and inconsistent. It would be impossible to use this technique to take data at high rates over long periods of time. The *calibration* (conversion of temperature rise to photon energy) is sensitive to the make-up of the lead block, the quality of the markings on the thermometer, and the disposition of the physicist. It is important to carefully calibrate the response of any detector in terms of physical quantities, and to make this calibration as stable as possible. There is no information provided by the detector about the shape of the absorbed shower, and the position of the photon is known only to be somewhere in the block. The shape of the shower is quite useful since it would tell us that the detected particle interacted electromagnetically in the detector. This is an important signature left by photons and electrons. We would need to segment the detector and read-out the temperature rise in each small subsection of the block in order to reconstruct the position and shape of the shower.
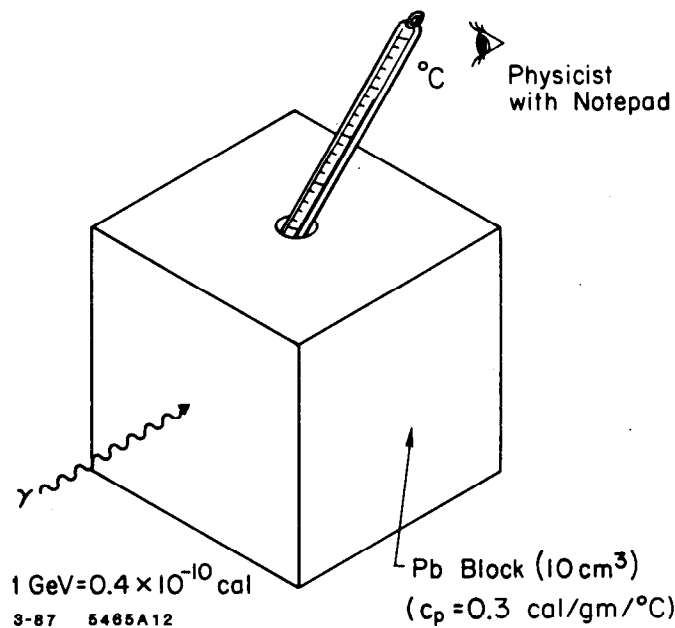

Fig. 20. A possible electromagnetic calorimeter.

An improvement in our design that addresses some of these drawbacks is shown in Fig. 21. In this case a gap is machined in the block at a depth that corresponds roughly to t_{max} for a 1 GeV shower. The physicist looks into the
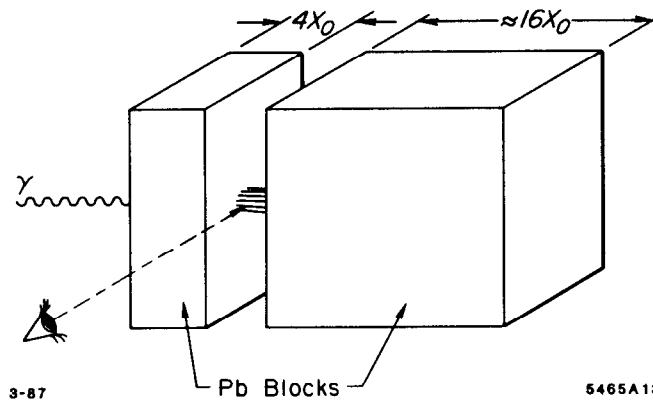
Fig. 21. An improvement on the design in Fig. 20.

gap and counts the number of charged particles, $N_{\max}$, created by the incident photon or electron. From the results of the previous section we expect that,

$$N_{\max} \approx 0.1 \cdot \frac{E}{\epsilon_c} \ . \tag{24}$$

The critical energy in lead is about 8 MeV (Fig. 16), so a 1 GeV incident particle produces $N_{\max} \approx 12$. The variation in this number from event to event is just $\sigma(N_{\max}) = \sqrt{12} \approx 3.5$, so the resolution with which the detector determines the photon energy is about 30%. This type of device is called a *sampling calorimeter*, and its performance can be summarized by noting that,

$$E_{\mathrm{measured}}(\mathrm{GeV}) \approx 0.08 \cdot N_{\mathrm{observed}} \tag{25a}$$

and

$$\frac{\sigma_E}{E} \approx \frac{\sqrt{N_{\mathrm{observed}}}}{N_{\mathrm{observed}}} \approx \frac{30\%}{\sqrt{E}} \ . \tag{25b}$$

The $E^{-1/2}$ behaviour of the resolution is characteristic of devices that rely on counting the number of particles in all or part of the shower to determine the energy of the shower. A refinement of this basic idea is to use repeated samplings of the shower as shown in Fig. 22. If the sampling is done at depths in the shower spaced by t_{sample} (in units of radiation lengths), then the average number of particles counted is given approximately by the rule-of-thumb,

$$N_{\mathrm{observed}} \approx \frac{50 \cdot E}{t_{\mathrm{sample}}}, \tag{26}$$

21

if E is given in GeV. So, for example, if $t_{\text{sample}} = 1X_0$ then a 1 GeV incident photon will yield $N_{\text{observed}} \approx 50$ and $\sigma \approx 15\% \cdot \sqrt{E}$. This is a typical performance characteristic of sampling calorimeters used in high-energy physics experiments.
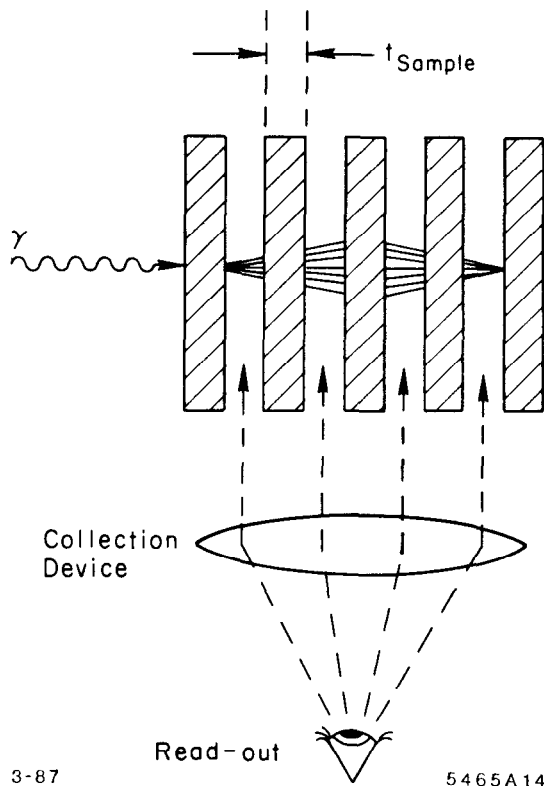

Fig. 22. A refinement of the design in Fig. 21.

g. Hardware Implementation

In the previous section we developed the concept of a sampling calorimeter. We saw that if we could count the number of charged particles that pass through gaps in the high-Z medium in which a shower is propagating we could reconstruct the total energy of the shower. The question is how to count shower particles. The usual technique is to fill the sampling gaps with a second, low-Z medium, and then measure the ionization left by the charged particles in the shower as they pass through this medium. A first example is shown in Fig. 23. The sampling gap is partitioned into cells by aluminum walls and filled with an appropriate gas mixture. Fine wires are strung through the centers of these cells and held at positive high-voltage relative to the aluminum walls. The free electrons created in the gaps by the shower particles will drift along the electric field lines to the sense

wire, where they initiate an avalanche in the extremely high electric field near the wire. This avalanche will result in $10^5 - 10^6$ electrons collected on the wire for each electron liberated in the gas by the shower. The total charge collected on the sense wires is a measure of the number of particles in the shower. This type of device is called a proportional wire chamber (PWC). A gas calorimeter used in a large experiment may have thousands of individual cells arranged to allow the position and detailed shape of the shower to be reconstructed. These devices have several draw-backs, however. Firstly, since the gas in the sampling cells is of very low density, the kinetic energies of non-relativistic components of the shower are large compared to the ionization created by the relativistic components. For example, a *minimum ionizing particle* (*i.e.*, a particle with $\gamma\beta \gg 1$) will lose only ≈ 1.3 keV as it passes through 1 cm of $ArCO_2$ gas at standard temperature and pressure. When a non-relativistic particle is brought to rest in the gas (for example if it travels parallel to the sense wire for a distance) it creates a large fluctuation in the pulse height observed on the sense wire. This degrades the energy resolution of the calorimeter. Also, the gas gain (the multiplicative factor of the gas avalanche) is very sensitive to changes in the pressure and temperature of the gas, so these devices must be very carefully calibrated quite frequently.
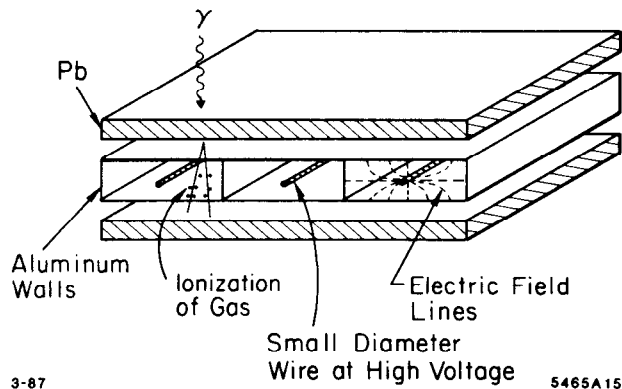

Fig. 23. A set of proportional wire cells. An electron-positron pair created by a photon incident on the upper lead converter is depicted passing through the left-most cell.

The difficulties of a gas calorimeter can be overcome by using a more dense material for the sampling medium. A common technique is to use strips of plastic scintillator attached to photomultiplier tubes as shown in Fig. 24. Visible light is emitted by the atoms of the scintillating material as the electrons liberated by the passage of a charged particle are recaptured. Some of these photons will propagate down the plastic strip and strike the photocathode of the photomultiplier tube. The photocathode is made of a material that is easily photoionized so

it readily converts the incident photons to electrons. These photoelectrons are attracted to the first dynode of the tube which is held at a voltage somewhat above that of the photocathode. By the time a photoelectron reaches the first dynode it has gained sufficient kinetic energy that it causes the release of several (typically 3-4) electrons from the dynode itself. This process repeats through a number of dynode stages (usually 10-12) until the charge is collected on the anode. The gain of the tube is the final charge collected on the anode per photoelectron emitted from the cathode, and is typically $\approx (3-4)^{12} \approx 10^{6-8}$. This technique for detecting charged particles is one of the oldest in experimental particle physics, but is still one of the best. Photomultiplier tubes produce a large signal-to-noise and calorimeters built with scintillator exhibit good linearity, resolution, and segmentation. The need to transport the light to photomultiplier tubes is sometimes mechanically difficult, however, and plastic scintillator is susceptible to aging and damage by radiation.
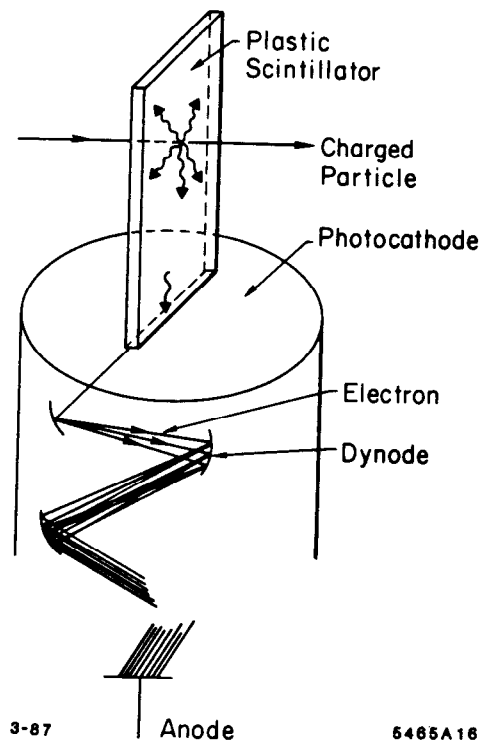
Fig. 24. A strip of scintillating plastic attached to a photomultiplier tube.

It is also possible to almost realize our initial idea of a thermometer in a block. This can be done by placing a photomultiplier tube on one face of a block

of lead glass (Fig. 25). Lead glass is the stuff crystal glassware is made from. The radiation length in lead glass is ≈ 3 cm and the optical index $n \approx 1.5$. It does not scintillate, but charged particles with velocities $\beta > \frac{1}{n} \approx 0.6$ will produce Cerenkov light which can be seen by the photomultiplier tube. In the geometry shown in the figure the pulse height from the phototube will be proportional to the total track length of charged particles in the shower with $\beta > 0.6$. The energy resolution of this detector is limited only by fluctuations in the low energy component of the shower, but $\sigma \approx 8\% \cdot \sqrt{E}$ is typical of well-calibrated systems. Unfortunately lead glass is very susceptible to radiation damage and is relatively expensive. These detectors are also mechanically difficult and it is hard to obtain complete 3-dimensional reconstruction of the shower.

Lead Glass Block

Photomultiplier Tube

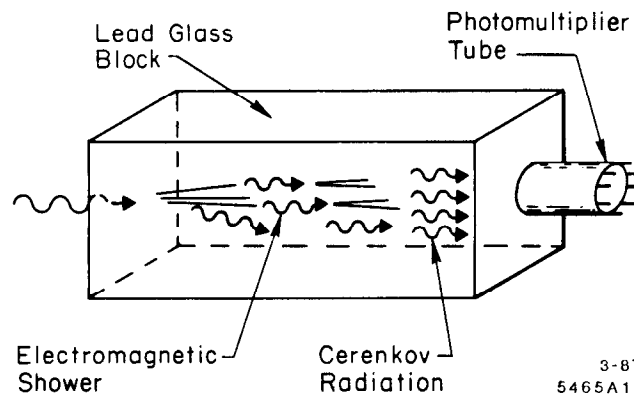Electromagnetic Shower

Cerenkov Radiation

3-87
5465A17

Fig. 25. A block of crystal lead-glass with a photomultiplier tube attached to one end.

Even better energy resolution can be obtained with scintillating crystals such as sodium iodide (NaI). These are optically transparent, high-Z scintillators that are sensitive to nearly all of the path length of charged particles in the shower. Although very expensive and not easy to work with, calorimeters made with these crystals have achieved energy resolutions that are almost that of an ideal detector (e.g., 1% at 1 GeV).

Table I is a summary of techniques in electromagnetic calorimetry.

2. NEUTRINO COUNTING EXPERIMENTS

Experiments at PEP and PETRA have reported results of searches for single-photon production by e^+e^- annihilation. The most sensitive of these is the ASP experiment at PEP. We will start this lecture with a discussion of the ASP apparatus to highlight the use of electromagnetic calorimetry in a high-energy physics experiment. Then we will focus on key aspects of the experimental

Table I. Hitchhikers Guide to Electromagnetic Calorimetry

Type	Resolution	Advantages	Disadvantages
Sampling:			
• gas	$20\%/\sqrt{E}$	fine segmentation, radiation hard	unstable gain
• scintillator	$15\%/\sqrt{E}$	fine segmentation, compact and rugged	susceptible to damage by radiation and aging
• liquid argon	$15\%/\sqrt{E}$	fine segmentation, stable gain	cryogenic
Lead glass	$8\%/\sqrt{E}$	good resolution	radiation, expensive, limited segmentation
Crystals Sodium Cesium BGO	$\approx 1\%$	optimal resolution	radiation, very expensive, limited segmentation

technique and interpretations of the results. Studies of single-photon even rates will also be of great interest at the SLC and LEP. In the last part of this lecture we will preview these measurements and try to prognosticate a bit on what will be known and when we will know it.

2.1a. The ASP Detector at PEP

The ASP detector is shown in Fig. 26. The central calorimeter is constructed of 632 lead-glass bars each with a photomultiplier tube on one end. These bars are arranged in 5-layer stacks that completely surround the beam-line in azimuth [Fig. 26(a)], and extend $\approx \pm 1$ meter along the beam direction in Z [Fig. 26(b)]. In this configuration an electromagnetic shower produced by a photon or electron that is created at the beam-beam interaction point (I.P.) will propagate perpendicular to the axis of the bars (not along the bar as in Fig. 25), and will span 5-10 lead-glass blocks. This is reasonably good segmentation, and allows the experimenter to reconstruct the position and direction in space that the incident particle was traveling when it entered the calorimeter. For example, Fig. 27 shows a Bhabha event $e^+e^- \to e^+e^-$ observed in the detector at PEP. In this picture each lead-glass bar is represented by a box, the size of which is scaled

to represent the energy that was observed in the bar. The two electromagnetic showers produced by the outgoing 14.5 GeV electrons are quite clear. It is easy to see that both of these showers originate at the I.P.
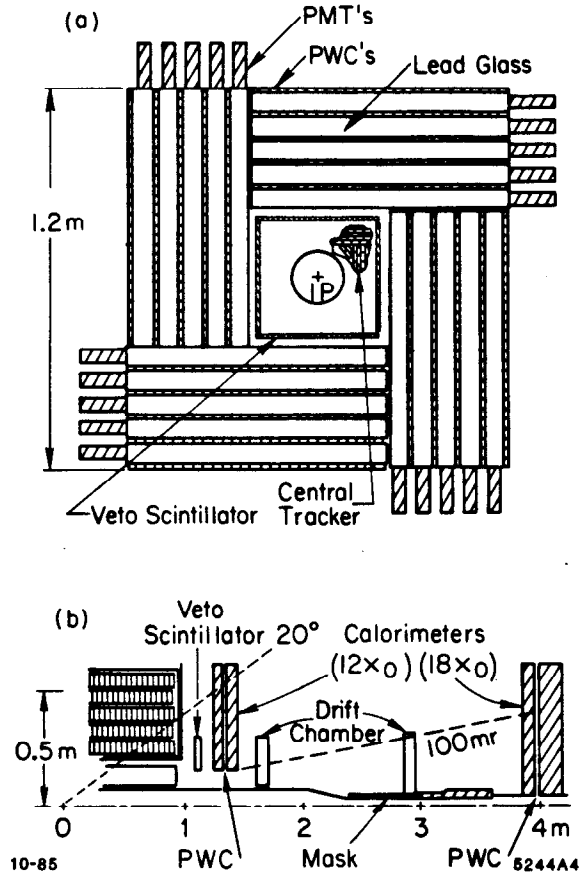

Fig. 26. (a) XY view of the ASP detector.
(b) YZ view of the ASP detector.

Notice that the lead-glass bars measure the XZ or YZ profile of an electromagnetic shower, but not the XY (azimuthal) profile. In order to complete the three dimensional reconstruction of the shower, the lead-glass bars are interleaved with PWC cells with sense wires that run perpendicular to the axis of the glass bars (c.f. Fig. 23). The ends of these cells can be seen in Fig. 26. The pulse-height observed in each PWC channel is also represented on event pictures by boxes of different sizes. For example, the XY view of the Bhabha event is shown in Fig. 28 and reveals the shower evolution in the calorimeter. Taken together, the lead-glass and PWC detectors allow a full three-dimensional reconstruction of electromagnetic showers. These components detect particles produced at the
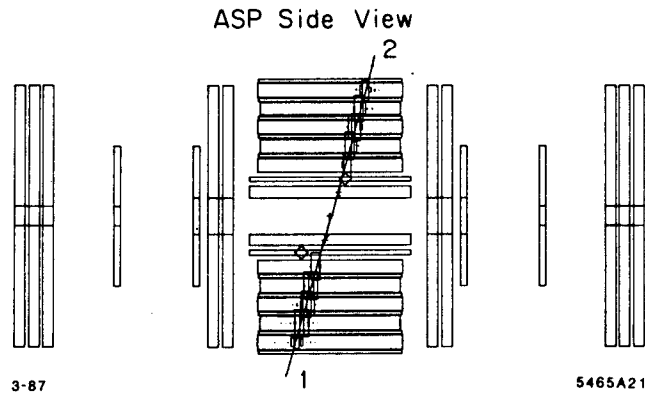
27

ASP Side View

Fig. 27. A Bhabha event $e^+e^- \longrightarrow e^+e^-$ observed in the ASP detector.
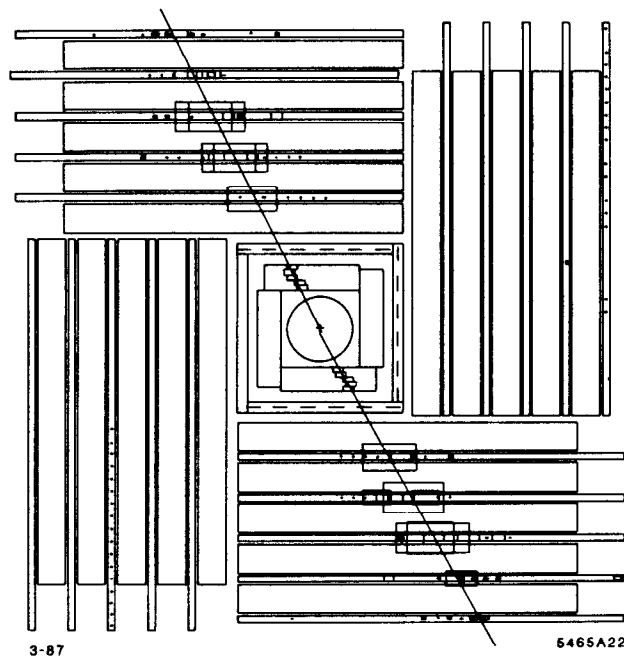

Fig. 28. XY view of the Bhabha event in Fig. 27.

I.P. with all azimuthal angles and $20° \leq \theta \leq 160°$. This defines the solid angle in which photons will be counted in the search for reaction (2).

Additional hardware components are required to complete the search for single-photon events. Certainly we must be able to distinguish signal photons from charged particles. This is done in the ASP experiment with a set of PWC cells placed between the beam-line and the central lead-glass calorimeter. This Central Tracker is shown in Figs. 26 and 29. The tracks produced in these cells by the charged e^+ and e^- pair are evident in the Bhabha event pictured in

Fig. 28. The Central Tracker cells that have been hit line up quite well with the showers observed in the PWCs in the calorimeter.
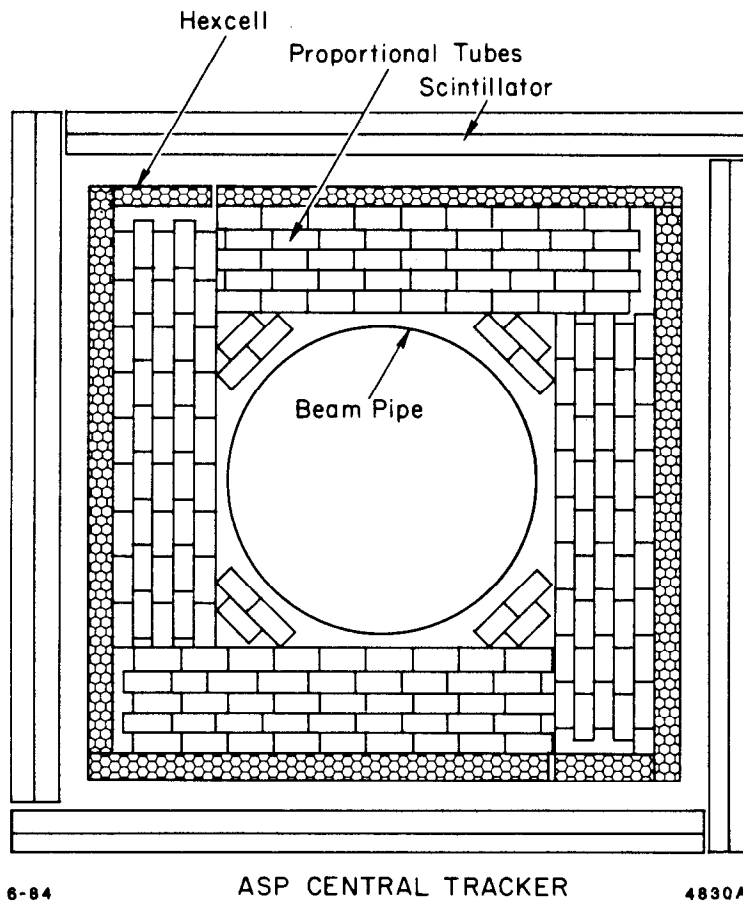

Fig. 29. Detail view of the ASP central tracker.

As we have discussed previously, it is also important to isolate true single-photon events from other e^+e^- processes by detecting any additional charged or neutral particle over essentially the complete solid angle around the I.P. The forward regions ($\theta < 20°$ and $\theta > 160°$) are covered in the ASP experiment [Fig. 26(b)] by sampling calorimeters made from lead and scintillator. Details of the mechanical structure of one of these modules are shown in Fig. 30. The thickness of each of these modules is $6X_0$ and the calorimeters shown in Fig. 26 are made of either 2 or 3 modules. PWC cells identical to those in the central calorimeter are placed between the modules that make up the calorimeters so that the production angles of high-energy forward particles can be measured. Figure 31 shows an example of a very important class of events – radiative Bhabha
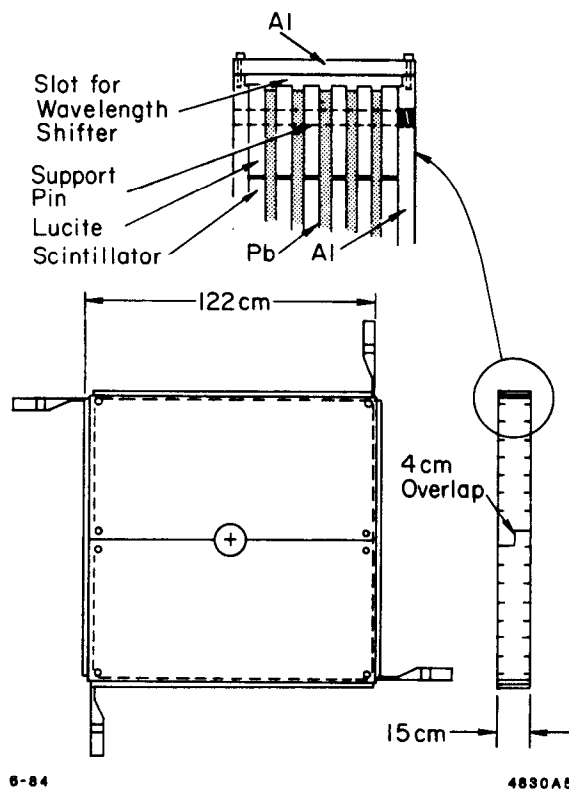
Fig. 30. Detail of lead-scintillator modules used in the
forward calorimeters of the ASP detector.

scatters,

$$e^+e^- \longrightarrow \gamma e^+e^- \quad . \tag{27}$$

The outgoing e^+ and e^- are detected by the PWC's in the forward shower modules and other tracking devices, and the photon shower is detected in the lead glass. These events are important because it is possible to kinematically fit them without using all of the measured quantities. For example if we measure the production angles of all three particles, then energy and momentum conservation (4 constraints) allow us to calculate the energies of the particles in the event (3 unknowns). This technique is used to determine the energy calibration and resolution of the calorimeters in the detector. These events can also be used to determine other properties of the shower reconstruction. The origin in space and time of photon candidates can be determined as the distance-of-closest-approach to the known I.P. (denoted by R), and the time of the lead-glass pulse measured with respect to the beam crossing time. These quantities provide extremely powerful discrimination of signal events from background due to cosmic rays, beam-gas

collisions, and debris created by stray beam particles that strike machine components. The distribution in R for signal events measured with photons from radiative Bhabha scatters is shown in Fig. 32. The resolution is $\sigma_R = 2.8$ cm. The timing resolution of the lead-glass pulse is $\sigma_T = 1.5$ nsec. We will use these variables shortly to examine the sample of candidate single-photon events in the ASP data.
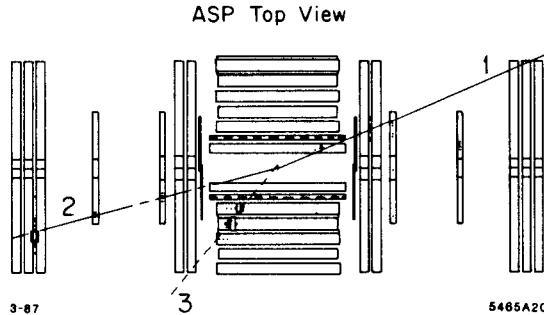
ASP Top View

Fig. 31. A radiative Bhabha event $e^+e^- \longrightarrow \gamma e^+e^-$ observed in the ASP detector.

In the PEP ring the electrons and positrons are each stored in three bunches that are about 3 cm in length. At a particular interaction point these bunches collide with each other 400 thousand times per second. This rate is far too high for the computer that controls the experiment to read out the electronics on each beam crossing, so it is necessary to select only those crossings which result in some visible energy in the detector. Fortunately this occurs at a very low rate. The computer read-out of the detector electronics is *triggered* when a fast analog sum of the pulse height in all lead-glass bars exceeds the equivalent of 1.5 GeV, or when the energy in a single quadrant, or adjacent quadrants, exceeds 0.6 GeV. This trigger occurs at the rate of approximately 5 Hz. While the electronics is being read out the experiment ignores the beam, so a trigger creates what is called "dead time". In this case, the experiment loses about 5% of the available beam time due to the event read-out. Since the trigger selects only 1 out of every 100,000 beam crossings, it must be shown that it doesn't throw away any signal events. This is again done with the radiative Bhabha events. These events are also selected by the trigger logic, but in a special way. Beam crossings that result in a large energy in the forward calorimeters, and any pulse height in the lead glass in excess of ≈ 200 MeV automatically trigger the computer. The trigger efficiency for single-photon events is measured by examining the sample of radiative Bhabha events to find those that also satisfy the single-photon trigger. This efficiency is found to be $> 99\%$ for photons in the fiducial region of the single-photon search ($\theta > 20°$) and with $p_t^\gamma > 1.0$ GeV/c.
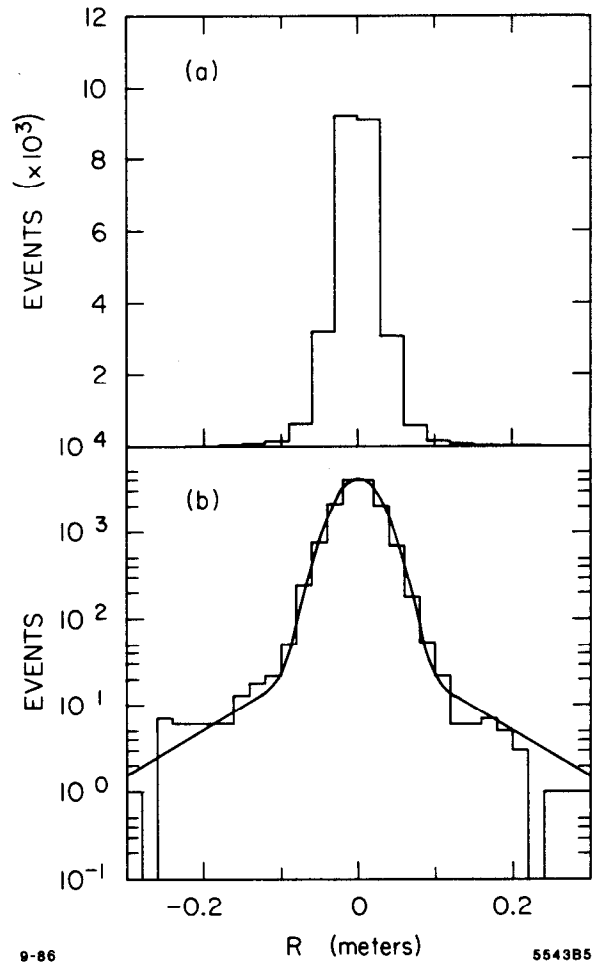
Fig. 32. Distance-of-closest-approach to the IP recon-
structed with radiative Bhabha events at PEP.

b. ASP Data Sample

The ASP experiment operated at PEP for two years. During that time it
logged an integrated luminosity of 115 pb^{-1} with 3 billion beam-crossings and
30 million triggers. The cross section for the standard weak interactions shown
in Fig. 2 is $\sigma_{\gamma\bar{\nu}\nu} = 0.032$ pb (for photons in the fiducial region given above), so
the experimenters were looking for an excess of events over the expected number
of 3-4.

The analysis of the triggers that were written to computer tape consists of
two parts: (1) First a cluster of lead-glass bars is found in which energy has been
deposited in a pattern that is recognized as an electromagnetic shower produced
by a photon created at the I.P. (2) Then every part of the detector is examined for
evidence of any other charged or neutral particle. Photon showers are recognized

as clusters that are continuous and have length and width consistent with that expected from an electromagnetic shower. Shown in Fig. 33 is an event that fails these requirements. Notice that there is a gap in the first layer of lead glass and the pattern of bars that contain energy is quite wide. (Compare with Fig. 31.) The probability that a single photon would create this pattern is very small. The lead glass signals in this event form two showers that are consistent with the two photons from the decay of a π^0. Photons created in radiative Bhabha events are used to measure the efficiency with which true signal events are accepted by these requirements. It is relatively easy to define criteria that strongly reject background events yet which accept 75-80% of the real photons.
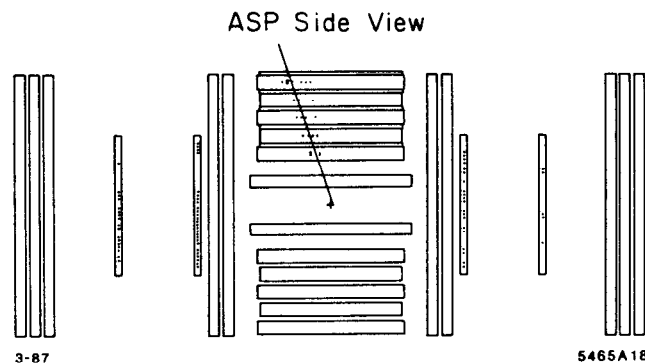
ASP Side View

3-87   5465A18

Fig. 33. A beam-gas π^0 candidate.

The complete solid angle coverage of the detector is crucial for the second half of the analysis. Triggers taken on randomly chosen beam crossings are used to see how sensitive the detector is to the presence of additional particles. This sensitivity will be limited by the *intrinsic noise* of the detector components, and by debris created by e^+e^- beam particles that stray from the normal beam orbit. Every component of the detector is examined on the random triggers for any evidence of energy or track segments that would have been left by a charged or neutral particle. Based on these studies cuts are defined that are then applied to the single-photon candidate events. For example, the energy observed in the forward shower counters and the energy in the lead-glass quadrants opposite the photon candidate must be essentially zero if the event is to be accepted as a single-photon candidate. The actual cut on the energy observed in the lead-glass quadrants not struck by the photon candidate is placed at 20 MeV. This is approximately the same signal generated by a minimum ionizing particle passing half-way through a single lead-glass bar. The combined isolation criteria are very sensitive to many sources of potential background, yet it is found that they reject

only 12% of all random beam crossings. The detector components were chosen in part because they all produce large signals with little intrinsic noise.

The analysis reduces the data sample to 250 single-photon candidate events. These events are displayed in Figs. 34 and 35. The events are nearly all in time with the beam crossing, but are spread broadly in R. With the exception of one event, the transverse momenta of these events are all small. The one event at $p_t^\gamma = 3.4$ GeV, shown in Fig. 36, is a beautiful single-photon event. The rest are consistent with the background of beam-gas that we discussed in Lecture I. The overall efficiency of the data analysis (photon pattern cuts and isolation criteria) is 60%, so we expect to see 2.2 single-photon events with $p_t^\gamma > 1$ GeV from the standard weak production of neutrino pairs. There is a 25% probability that zero or one event will be observed in an experiment in which 2.2 are expected, so the *confidence level* of the observed result is quite reasonable.
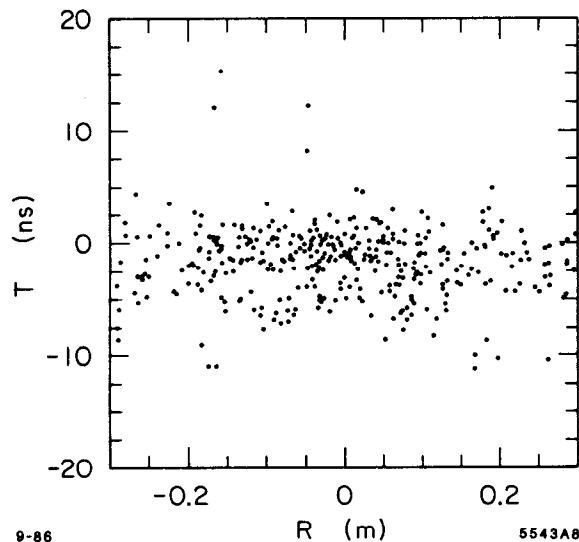
Fig. 34. Distribution of R and T of candidate single-photon events with $p_t^\gamma > 0.5$ GeV.

c. Limits on the Number of Neutrino Generations

The observation of one single-photon event in the ASP data sample can be used to place a limit on the cross section for reaction (2). The value of the cross section that would reduce the confidence level of the observation to 10% is taken to be the 90% confidence level upper limit placed on the cross section by the
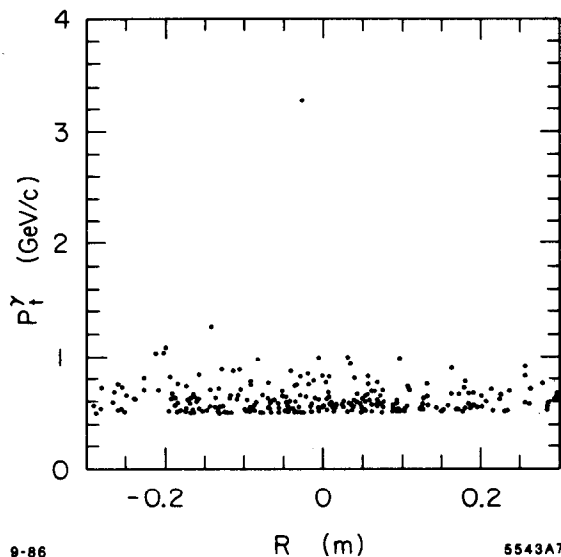
Fig. 35. R and p_t^γ distribution of events in Fig. 34.
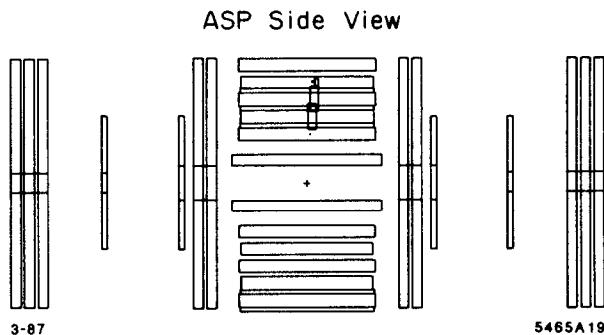
ASP Side View

Fig. 36. Single-photon event observed with $p_t^\gamma = 3.4$ GeV/c.

existence of the observation. This value is found to be

$$\sigma(e^+e^- \rightarrow \gamma + \text{weakly interacting particles}) < 0.054 \text{ pb} \qquad (28)$$

for $E_\gamma < 10.5$ GeV, $p_t^\gamma > 1$ GeV and $\theta^\gamma > 20°$.

By comparison, the standard weak processes produce a cross section of 0.032 pb, and it is straightforward to find that the limit (28) corresponds to $N_\nu < 7.5$. A comparison of this limit with all other reported results[12-14] is given in Fig. 37. When combined with results from other e^+e^- experiments, the overall limit on N_ν is 4.9. The three experiments ASP, MAC, and CELLO observe 2 events between them; 3 neutrino generations should have produced 4 events in

their combined data sample. Notice that this doesn't rule out the possibility that there are 5 neutrino species (or any other number for that matter). It simply means that if there are 4.9 equivalent neutrino generations then there is only a 10% chance that the three experiments would see 2 or less events. The limits from e^+e^- experiments are very general — they depend only on the assumption that neutrinos couple with universal strength to the weak charged and neutral currents as prescribed by the Standard Model (and on radiative corrections to Eq. (3)).
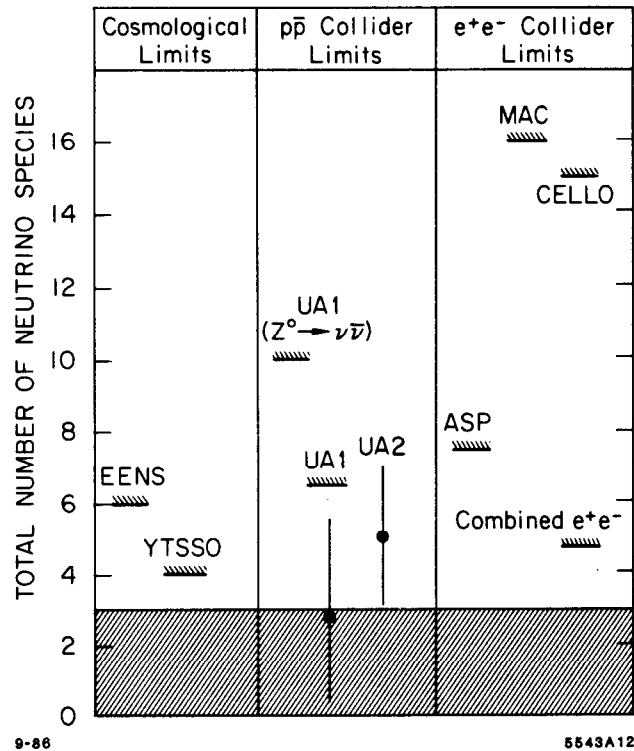
Fig. 37. Summary of present limits on N_ν.

Limits also shown in Fig. 37 have been reported[14] from studies of $\bar{p}p$ collisions at CERN. These experiments are able to place upper limits on the total width of the Z^0 and hence limits on the partial width $\Gamma(Z^0 \rightarrow \bar{\nu}\nu)$. Measurements are made of the ratio,

$$R \equiv \frac{\sigma(\bar{p}p \rightarrow Z + X) \cdot BR(Z \rightarrow e^+e^-)}{\sigma(\bar{p}p \rightarrow W + X) \cdot BR(W \rightarrow e\nu)} \qquad (29)$$

which is just the number of Z^0's and $W^\pm$'s observed in the electron decay channel

by the UA1 and UA2 experiments. This ratio can also be written,

$$R = \frac{\sigma(Z)}{\sigma(W)} \cdot \left(\frac{\Gamma_W}{\Gamma_Z}\right) \cdot \left(\frac{\Gamma_{Z \to ee}}{\Gamma_{W \to e\nu}}\right) \qquad (30)$$

If we compute everything in expression (30) except Γ_Z, and measure the ratio R, then the total width of the Z^0 can be deduced. This technique relies on the assumption that the total width of the $W^\pm$ does not depend on the number of neutrino generations. This will be true if the neutrino in question is in a weak iso-doublet with a charged partner that is too heavy to be produced in W decay. This technique will fail if there is any other unknown contribution to the W total width. The QCD calculation of the ratio of Z^0 and $W^\pm$ production rates relies on knowledge of the proton structure function at relatively low x (typically $x \approx 0.15$), and of course, on the value of $\alpha_s(Q^2)$. The value of Γ_Z found in this way is compared with the expected Z^0 width in the absence of any other decay channels to arrive at the limits shown in the figure. These limits are numerically competitive with those from e^+e^-, but clearly require more theoretical input.

d. **Limits on SUSY**

The limit on the cross section (28) can also be used to place limits on processes such as those in Fig. 3 that are predicted to occur in theories of Supersymmetry. Calculating these limits is a bit more complicated due to the presence of single-photon events from the 3 known neutrino species. This process now constitutes a background. There are two schools of thought on how to treat this situation in the case of small numbers of events.[15] A *classical* statistical procedure consists of computing the probability that the observation of the experiment occurred if the hypothesis being tested is true, while a *Bayesian* analysis will attempt to compute the probability that a particular hypothesis is true given that the observation of the experiment was made. (You might want to read that sentence again.) The classical procedure is straightforward, but is unacceptable to some because it does not attempt to pass judgment on the validity of the hypothesis in question. In a Bayesian analysis, on the other hand, probabilities are interpreted as "degrees of rational belief", and an attempt is made to compute these probabilities. In many cases these two become equivalent although they would lead to different interpretations of the result. For example, the limit on N_ν quoted for the ASP result can be viewed as the value of N_ν that reduces the probability of the experimental observation to 10% in a classical interpretation, while a Bayesian analysis would argue that the existence of the observation implies that there is only a 10% chance that the real value of N_ν is greater than 7.5. The details of the two approaches yield the same numerical value.

This is not the case, however, when the hypothesis under scrutiny contains two sources of events — call one signal and the other background. For example, if we assume that there are, in fact, three neutrino types then it is possible that an experiment like ASP could observe so few events that the probability of the observation (or confidence level of the experiment) could be less than 10%! This probability will become even less if we hypothesize that there is a non-zero cross section for production of SUSY particles in addition to the standard weak processes. There is nothing inconsistent in this, but if the classical confidence level of the experiment becomes too small for an hypothesis that is thought to be true, then the experimenter is either very unlucky or has done something wrong, or the hypothesis is not really true in the first place.

In a Bayesian analysis a probability distribution is used to parameterize the experimenter's *a priori* knowledge of the hypothesis under study — that is, before the experiment was performed. For example, it may be assumed that all numbers of signal events are *a priori* equally likely, or that all values of a particular physical parameter are equally likely. (Note that if the cross section is not linear in the physical parameter in question, then these two are not equivalent assumptions.) The calculation then yields the *a posteriori* probability for the physical quantity to lie in any particular region given that the experimental observation was made. For example, if the ASP, MAC, and CELLO experiments had observed zero events (remember that they expected to see 4 if $N_\nu = 3$), then a Bayesian analysis with the *a priori* assumption that all numbers of detected events are equally likely would lead to the conclusion that the SUSY contribution to the single-photon cross section corresponds to less than ≈ 2.3 detected events at 90% confidence level. This could be used to compute a limit on a physical quantity (*e.g.*, the selectron mass), but it should be kept in mind that the classical probability of the three experiments observing zero events is only 1.8% even if there is no production of SUSY particles at all.

It should be clear that proper interpretation of an experimental result requires knowledge of both the experimental data and the sensitivity of the experiment. For the case at hand it was stated earlier that there was a 25% probability that the ASP experiment would observe one or fewer events if $N_\nu = 3$. If we assume that there is an additional contribution to the single-photon cross section then this probability will become smaller. If the $\widetilde{\gamma}$ is the lightest SUSY particle,[6] then this probability is 10% for a selectron mass $m_{\tilde{e}} = 67$ GeV/c^2 (with $m_{\widetilde{\gamma}} = 0$ and degenerate $\tilde{e}$ mass states), and 5% for $m_{\tilde{e}} = 59$ GeV/c^2. Under the alternative hypothesis[16] that the $\tilde{\nu}$ is the lightest SUSY particle (and that there are three massless $\tilde{\nu}$ generations), this probability is 10% for $m_{\widetilde{W}} = 69$ GeV/c^2, and 5% for $m_{\widetilde{W}} = 60$ GeV/c^2. A Bayesian analysis with the *a priori* assumption that

all values of the expected number of SUSY events (N_{SUSY}) are equally likely yields the 90% CL limit $N_{SUSY} < 3.2$ events. The corresponding limits on the $\tilde{e}$ and $\tilde{\gamma}$ masses are shown in Fig. 38. For three massless $\tilde{\nu}$ generations, the 90% CL on the mass of the $\widetilde{W}$ is $m_{\widetilde{W}} > 61$ GeV/c^2, and the 95% CL limit is $m_{\widetilde{W}} > 57$ GeV/c^2.
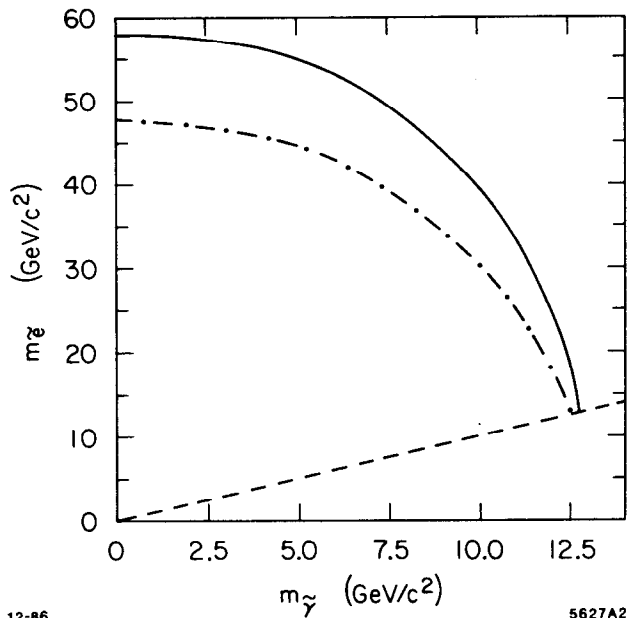

Fig. 38. Limits (90% CL) placed on $\tilde{e}$ and $\tilde{\gamma}$ masses by the ASP experiment. The solid line is for degenerate $\tilde{e}$ masses and the dash-dotted line is the limit if only one mass eigenstate contributes to the cross section.

2.2 Neutrino Counting at SLC and LEP

The SLC and LEP are e^+e^- colliding beam machines designed to operate at center of mass energies near the Z^0 mass. At these machines it will be possible to determine precisely the coupling of the Z^0 to stable weakly-interacting neutral particles. This can be done either by direct measurment of the partial width $\Gamma(Z^0 \to \bar{\nu}\nu) \equiv \Gamma_{\bar{\nu}\nu}$ or by measurement of the total width of the Z^0.

a. The Z^0 Total Width

The total width of the Z^0 can be written,

$$\Gamma_{\text{tot}} = \frac{G_F m_Z^3}{24\sqrt{2}\pi} \left\{ 2 \cdot N_\nu + \left[1 + (1 - 4\sin^2\theta_W)^2 \right] N_\ell + \left(1 - \frac{\alpha_s(m_Z)}{\pi} + O(\alpha_s^2) \right) \right.$$

$$\left. \cdot \left[(2 + \rho(m_t)) \left(1 + \left(1 - \frac{8}{3}\sin^2\theta_W \right)^2 \right) + 3 \left(1 + \left(1 - \frac{4}{3}\sin^2\theta_W \right)^2 \right) \right] \right\} \quad (31)$$

where $\rho(m_t)$ is the phase space available for the decay of the Z^0 to top quark pairs (normalized to that of a massless quark), and we have assumed that the only other unknown is the number of massless neutrino species. In addition to the QCD radiative corrections that are explicitly shown, we also need to make electroweak radiative corrections to this expression. If we take the mass of the Z^0 to be 93 GeV, $\alpha_s = 0.12$, the mass of the top quark to be 40 GeV, and $N_\nu = 3$, then

- $\Gamma_{\text{tot}} = 2.74$ GeV,
- $\Gamma_{\bar{\nu}\nu} = 0.176$ GeV per species (6.4% per species),

and the radiative corrections have been estimated[17] to be,

- Electroweak corrections ≈ -0.075 GV,
- QCD corrections $\approx +0.085$ GeV.

The radiative corrections are each equivalent to about $\frac{1}{2}$ of a neutrino generation in their effect on the total width, but to the accuracy that they are known, they fortuitously nearly cancel each other.

A measurement of the total width can be made by scanning the beam energy across the Z^0 peak and fitting the observed excitation curve to the expected shape. It is essential that radiative corrections to the shape be fully understood if a meaningful width is to be obtained in this way. If we then assume that all contributions to the width are known except that due to neutrinos, then the value of N_ν can be determined from the measured width and Eq. (31). It has been estimated[18] that the initial scan of the Z^0 peak at the SLC will determine the mass, width and peak cross section with accuracies,

- $\delta m_Z \approx 45$ MeV
- $\delta\Gamma_{\text{tot}} \approx 135$ MeV (compared to 175 MeV per neutrino species)
- $\delta\sigma_{\text{peak}} \approx 3.5\%$.

With these uncertainties it will not be possible to distinguish 3 neutrino generations from 4 with confidence, but it will be possible to place limits $N_\nu < 4$-5 that

are comparable to those from lower energy experiments (Fig. 37). Ultimately it will be possible to determine Γ_{tot} to $\approx$ 40-50 MeV at the SLC and perhaps 20-30 MeV at LEP.[17] (Storage rings have a small beam energy spread since the orbit of the ring strongly selects monochromatic bunches of electrons and positrons.) This will lead to an experimental accuracy that corresponds to $\approx$ 0.3 (perhaps 0.2) neutrino generations.

b. $\Gamma_{\bar{\nu}\nu}$ Partial Width

We would really like to determine the partial width of the Z^0 decay to neutrino pairs (or neutrino-like objects) directly in order to improve the sensitivity of the measurement and to avoid the assumptions inherent in the use of Eq. (31) to deduce this quantity. One possible way to do this is to measure both the total width of the Z^0 and the partial width $\Gamma_{Z\rightarrow\text{visible}}$ for decays into all final states except neutrinos. The partial width $\Gamma_{\bar{\nu}\nu}$ can then be obtained by subtraction,

$$\Gamma_{\bar{\nu}\nu} \equiv \Gamma_{\text{tot}} - \Gamma_{\text{visible}} \; . \tag{32}$$

The difficulty with this is that we are subtracting two large numbers to obtain a small one, so the two large numbers must be obtained with high precision,

$$\left(\frac{\delta\Gamma_{\bar{\nu}\nu}}{\Gamma_{\bar{\nu}\nu}}\right) \approx 5 \cdot \left[\left(\frac{\delta\Gamma_{\text{tot}}}{\Gamma_{\text{tot}}}\right)^2 + \left(\frac{\delta\Gamma_{\text{visible}}}{\Gamma_{\text{visible}}}\right)^2\right]^{\frac{1}{2}} \; . \tag{33}$$

This will be a useful technique only if both Γ_{tot} and Γ_{visible} can be determined to better than 2%.

The most general way to determine $\Gamma_{\bar{\nu}\nu}$ is to study single-photon production. The experiment is done[19] by operating the machine at a center of mass energy above the Z^0 mass. Initial-state radiation results in events of the type

$$e^+e^- \rightarrow \gamma Z^0 \quad \text{followed by} \quad Z^0 \rightarrow X \; , \tag{34}$$

which produce a photon spectrum characteristic of the Z^0 mass and width and the chosen beam energy. Spectra for several center of mass energies are shown in Fig. 39. The choice of beam energy is a compromise between optimization of the event rate and minimization of systematic errors due to uncertainty in the energy calibration of the detector. For example, if a cut on the energy of observed photons is made at a fixed value, $E^{\gamma}_{\text{min}} = 1$ GeV, then the total accepted cross section depends on E_{cms} as shown in Fig. 40. The peak cross section of 195pb occurs at $E_{\text{cms}} = 95$ GeV. As E^{γ}_{min} is increased, the position of the peak increases and its amplitude decreases. If we use a cut of $E^{\gamma}_{\text{min}} = 2$ GeV, rather than 1 GeV, the peak cross section would be 125 pb and would occur at approximately 97 GeV.

Running close to the Z^0 mass optimizes the peak. Conversely, the photon energy distribution produced at different center of mass energies (Fig. 39), becomes less steep with increasing beam energy. When the center of mass energy is more than $\Gamma_{\text{tot}} \approx 2.7$ GeV above the mass of the Z^0, a clear reflection of the Z^0 excitation curve is visible. The systematic uncertainty in the accepted cross section caused by uncertainty in the energy calibration of the detector can largely be eliminated by choosing E_{cms} and E^{γ}_{min} large enough to avoid the steep photon spectra seen in Fig. 39 at values of E_{cms} near the mass of the Z^0. Setting the machine center of mass energy to ≈ 3 GeV above the Z^0 mass appears to be the ideal compromise.
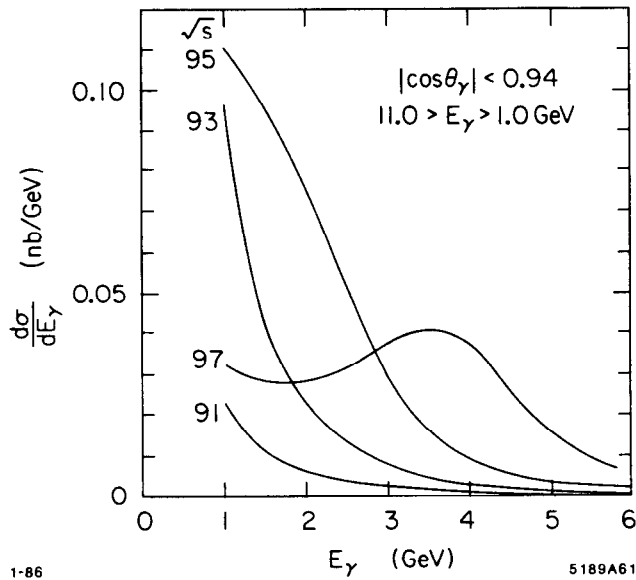

Fig. 39. Photon spectra produced by the standard weak processes with $N_{\nu} = 3$. Curves are for center of mass energies as labelled. The mass of the Z^0 is assumed to be 93 GeV and its width 2.7 GeV.

Since this experiment is optimally done at a center of mass energy above the Z^0 peak it will be in conflict with many of the other goals of the experimental groups working at SLC and LEP. Counting single-photon events in data samples taken at center of mass energies near the Z^0 peak will still yield reasonably good results, however. When combined with measurements of the total Z width and Γ_{visible} it will almost certainly be possible to distinguish 3 generations of massless neutrinos from 4. But if we take a more strategic view of the physics, then we will want to determine the partial width of the Z^0 to neutral weakly-interacting particles as precisely as possible. A single-photon counting experiment running for several months at the optimal center of mass energy above the Z^0 mass, and
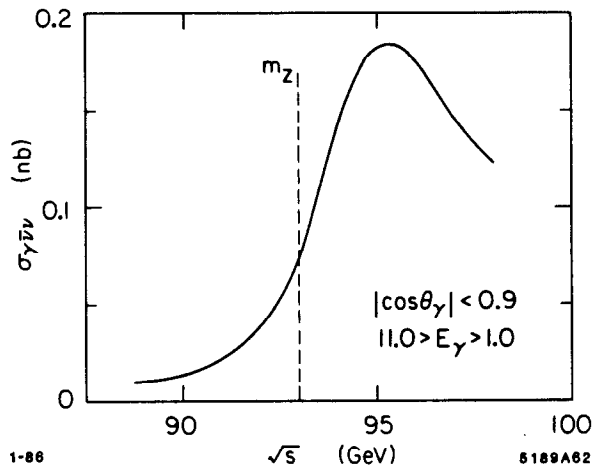
Fig. 40. Visible cross section for single photons from the process $\gamma\nu\bar{\nu}$ with $N_\nu = 3$.

with an average luminosity of 10^{30} cm^{-2} sec^{-1} at the SLC or LEP should be able to measure $\Gamma_{\bar{\nu}\nu}$ with an accuracy of 5% or better (*i.e.*, 0.15 generations of neutrinos). As a benchmark, remember that a light scalar neutrino $\tilde{\nu}$ contributes only half as much to the width of the Z^0 as does a light Dirac neutrino. (See Section 1.2.) It seems possible that an experiment dedicated to the study of this physics could measure $\Gamma_{\bar{\nu}\nu}$ sufficiently well to uncover the presence of such a particle.

REFERENCES

1. E. Ma and J. Okada, *Phys. Rev. Lett.* **41**, 287 (1978).

2. K.J.F. Gaemers, R. Gastmans and F.M. Renard, *Phys. Rev.* **D19**, 1605 (1979).

3. D.L. Burke, *Signatures of Supersymmetry in e^+e^- Collisions*, SLAC-PUB-3911, SLAC Summer Institute (1985); H.E. Haber and G.L. Kane, *Phys. Rep.* **117**, 76 (1985).

4. J. Ellis and J.S. Hagelin, *Phys. Lett.* **122B**, 303 (1983).

5. P. Fayet, *Phys. Lett.* **86B**, 272 (1983); G.L. Kane and J.P. Leveille, *Phys. Lett.* **112B**, 227 (1982).

6. K. Grassie and P.N. Pandita, *Phys. Rev.* **D30**, 22 (1984).

7. D. Dicus, *Phys. Rev.* **D21**, 1762 (1980).

8. Most of the results in this and the following subsections can be found in the Particle Data Booklet, *Phys. Lett.* **170B**, 44 (1986), and references therein.

9. B. Rossi, *High Energy Particles*, Prentice Hall (1952).

10. S. Iwata, Nagoya Print – DPNU-3-79, TRISTAN Workshop (1979).

11. W.R. Nelson, H. Hirayama and D.W.O.Rogers, *The EGS4 Code System*, SLAC-Report-265 (1985).

12. J. Yang *et al.*, *Astrophys. J.* **281**, 493 (1984); J. Ellis *et al.*, *Phys. Lett.* **167B**, 457 (1986).

13. C. Hearty *et al.*, ASP Collaboration, SLAC-PUB-4114 (1987); G. Bartha *et al.*, ASP Collaboration, *Phys. Rev. Lett.* **56**, 685 (1986); W.T. Ford *et al.*, MAC Collaboration, SLAC-PUB-4003 (1986); W.T. Ford *et al.*, MAC Collaboration, *Phys. Rev.* **33D**, 3472 (1986); H.-J. Behrend *et al.*, CELLO Collaboration, DESY Report 86-050 (1986).

14. S. Geer *et al.*, UA1 Collaboration, CERN-EP/86-115 (1986); J. Appel *et al.*, UA2 Collaboration, *Z. Phys.* **C30**, 1 (1986).

15. W.T. Eadie *et al.*, *Statistical Methods in Experimental Physics* (American Elsevier, New York, 1971), Sect. 2.2.5; H.B. Prosper, *Nucl. Instrum. Methods* **A241**, 236 (1985); V.L. Highland, Temple Preprint C00-3539-38 (1986).

16. J.A. Grifols, M. Martínez and J.Solà, *Nucl. Phys.* **B268**, 151 (1986).

17. G. Altarelli *et al.*, CERN 86-02 (LEP "Yellow Book"), p. 3 (1986).

18. G. Feldman, MarkII/SLC Physics Working Group Note 0-2, Asilomar, 1986.

19. G. Barbiellini, B. Richter and J.L. Siegrist, *Phys. Lett.* **106B**, 414 (1981).